Drag and interfacial vorticity of spherical bubble contaminated with soluble surfactant

Hayashi, Kosuke
Motoki, Yuya
Legendre, Dominique
Tomiyama, Akio

(Citation)
International Journal of Multiphase Flow,187:105173

(Issue Date)
2025-06

(Resource Type)
journal article

(Version)
Version of Record

International Journal of Multiphase Flow 187 (2025) 105173

Contents lists available at ScienceDirect

International Journal of Multiphase Flow

journal homepage: www.elsevier.com/locate/ijmulflow

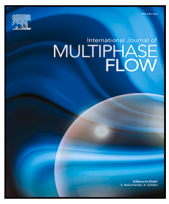

Research paper

Drag and interfacial vorticity of spherical bubble contaminated with soluble surfactant

Kosuke Hayashi [a],*, Yuya Motoki [a], Dominique Legendre [b], Akio Tomiyama [a]

[a] Graduate School of Engineering, Kobe University, 1-1 Rokkodai Nada, Kobe, 657-8501, Hyogo, Japan
[b] Institut de Mécanique des Fluides de Toulouse (IMFT) - Université de Toulouse, CNRS-INPT-UPS, Allée du Professeur Camille Soula, 31400, Toulouse, France

ARTICLE INFO

Keywords:
Bubble interface contamination
Numerical simulation
Stagnant-cap angle
Drag-vorticity relation

ABSTRACT

Numerical simulations of spherical bubbles contaminated with soluble surfactant were carried out to investigate the surfactant effects on the drag coefficient, C_D, and the interfacial vorticity, ω, produced at the bubble interface. The different surface contamination regimes are considered in both the diffusion-dominant case and advection-dominant case, for different ambient contamination conditions controlled by varying the Marangoni, Langmuir and Hatta numbers, Ma, La and Ha. The combinations, $\Pi_M = LaMa$ and $\Pi_H = Ha/La$, of the dimensionless groups were found to play dominant roles in the surfactant effects on C_D and ω in both cases. Four different regimes for the dependence of the drag force and vorticity distribution as a function of the above dimensionless group were identified. In the diffusion-dominant case the vorticity is well correlated with a weighting average for those of clean and fully-contaminated bubbles, and a linear relation between C_D and the maximum vorticity holds as in the case with clean bubbles. The characteristics of C_D in the advection-dominant case are more complicated, but they have been classified into four regimes in terms of Π_M and Π_H. A simple correlation of the stagnant-cap angle expressed in terms of Π_M was also obtained. This study thus revealed the surfactant effects on C_D and ω and the drag-vorticity relations in detail at the first time for the different regimes of surface contamination.

1. Introduction

The drag force acting on a bubble has been one of the main subjects in the multiphase flow research and there are a large number of studies on the drag coefficient, C_D (Clift et al., 1978; Maxworthy et al., 1996) (see Section 4.1 for its definition). As is well known, C_D of clean spherical bubbles at low and high bubble Reynolds numbers are both inversely proportional to the Reynolds number (Hadamard, 1911; Rybczynski, 1911; Levich, 1962). Legendre (2007) showed that C_D of the Stokes drag for solid sphere, the Hadamard–Rybczynski drag for clean fluid sphere at low Reynolds number and the Levich drag for infinite Reynolds number bubbles (Clift et al., 1978) are integrated in a single expression in terms of the Reynolds number and the maximum surface vorticity, and he also showed that a deformation effect can also be introduced in a similar form. Adoua et al. (2009) demonstrated the role of the surface vorticity in the lift reversal process for bubble in linear shear flow. The relation between the maximum vorticity and the drag was utilized in modeling the lift coefficients of clean bubbles rising in linear shear flows, in particular to describe the reversal of the lift force (Hayashi et al., 2020, 2021).

The presence of surfactant (surface-active agent) affects the motion of a bubble (Levich, 1962; Clift et al., 1978; Dukhin et al., 1995). Surfactant dissolved in liquid adsorbs to the interface of a bubble and its interfacial concentration is not uniform due to interfacial advection, resulting in a gradient of the surface tension, i.e., the Marangoni stress, which balances with the viscous shear stress at the interface. In the limiting case of fully-contaminated state the interface of a spherical bubble is immobile and the rise motion is similar to that of a solid sphere. Takagi and Matsumoto (2010) pointed out that the surfactant influences not only the single bubble motion but also the structure of a bubbly flow. Recently, Atasi et al. (2023) studied the stability of a bubble chain in carbonated drinks such as champagne, sparkling wine and beer and obtained a stability map for three dimensionless groups representing the bubble deformation and the degree of contamination. The authors demonstrated that the interfacial vorticity plays a crucial role in the bubble chain stability and was the key parameter to consider to provide a stability criterion. The interfacial vorticity thus facilitates understanding the bubble dynamics such as drag and lift effects and is expected to have a potential to reveal a relation between these forces and the relevant dimensionless groups for contamination in a simple

* Corresponding author.
E-mail address: hayashi@mech.kobe-u.ac.jp (K. Hayashi).

https://doi.org/10.1016/j.ijmultiphaseflow.2025.105173
Received 21 November 2024; Received in revised form 16 January 2025; Accepted 10 February 2025
Available online 17 February 2025

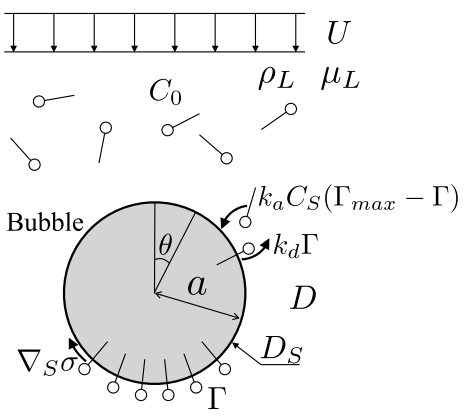

Reynolds number
$Re = \rho_L U d/\mu_L$
Langmuir number
$La = k_a C_0/k_d$
Marangoni number
$Ma = R_G T\Gamma_{max}/\mu_L U$
Hatta number
$Ha = k_a C_0 d/U$
Bulk and interfacial Peclet numbers
$Pe = Ud/D \quad Pe_S = Ud/D_S$
Dimensionless adsorption length
$K = \Gamma_{max}/C_0 d$

Fig. 1. Spherical bubble in uniform flow of contaminated liquid. Parameter and non-dimensional number definition.

form.

Savic (1953) introduced the stagnant-cap angle, θ_{cap}, to express an intermediately contaminated state of a bubble, where $\theta_{cap} = \pi$ for fully mobile interface while $\theta_{cap} = 0$ for fully immobile interface. For $0 < \theta_{cap} < \pi$, the bubble interface is partly immobile, while the remaining part is mobile due to the advection of surfactant at the interface (see Fig. 1). Sadhal and Johnson (1983) analytically investigated the interfacial velocity profile of a low Reynolds number drop for a given stagnant-cap angle. They derived the drag force expressed in terms of the cap angle θ_{cap}, which reduces to the result obtained by Harper (1982) for small immobilized region. Lerner and Harper (1991) applied the stagnant-cap model to two bubbles under interaction in the Stokes flow regime. Ramírez-Muñoz et al. (2012) carried out numerical simulations of stagnant-cap bubbles of the bubble Reynolds number Re (as defined in Eq. (3) and Fig. 1) ranging from 50 to 200. The normalized drag coefficient ξ (as defined in Eq. (45)) was empirically correlated with the cap angle. The stagnant-cap model has also been utilized in modeling the mass transfer from a contaminated bubble and particle-bubble interaction (Takemura and Yabe, 1999; Dani et al., 2006, 2022; Legendre et al., 2009).

For a bubble at intermediate degree of contamination, knowledge on the effects of the relevant dimensionless groups for the drag is required to develop drag coefficient correlations, though the stagnant-cap model successfully gives the drag and mass transfer coefficients for a predetermined cap angle as reviewed above. In numerical simulations carried out by Mclaughlin (1996) insoluble surfactant adsorbing to the interface of a deformed ellipsoidal bubble was considered. The rise velocity of the bubble was almost constant until the cap angle becomes large enough to cause the separation of flow. Cuenot et al. (1997) carried out numerical simulations of spherical bubbles in contaminated liquids at a high Péclet number Pe (as defined in Fig. 1 and Eq. (7)) by solving both transport equations of the surfactant concentrations in the liquid and at the interface. The state of contamination was classified into the following four categories from a point of view of interface state (IS):

- (IS-a): unretarded velocity profile with no impact of the surface contamination on the interface mobility,
- (IS-b): uniformly retarded velocity profile with a uniformly distributed reduction of the surface mobility,
- (IS-c): stagnant cap separating the interface into a mobile interface on the bubble front and an immobile surface at the rear of the bubble,
- (IS-d): completely stagnant with an interface completely immobilized as observed for a rigid sphere.

At the high Péclet number the bubbles under intermediately contaminated conditions tended to take the stagnant-cap state, and their drag coefficients were confirmed to be strongly related with the stagnant-cap angle. Takagi et al. (2003) also numerically studied the rise motion of a contaminated bubble. They showed that surfactant of small desorption rate affects the bubble rise velocity even at a small bulk concentration. Numerical simulations of spherical bubbles contaminated with soluble surfactant were conducted by Wang et al. (2002), in which the surfactant was utilized for controlling the formation and size of wake behind a bubble. Interface-capturing methods have been coupled with the surfactant transport equations (James and Lowengrub, 2004; Xu et al., 2006). Hayashi and Tomiyama (2012) used the level set method and pointed out that the Hatta number Ha (Fig. 1, Eq. (11)) plays an important role in determination of the degree of surfactant effect on the rise velocity of a Taylor bubble in a vertical pipe. Kurimoto et al. (2013) used the same numerical method to study the surfactant effect on the shape and the rise velocity of a Taylor drop. Kentheswaran et al. (2023) used the level set method (Kentheswaran et al., 2022) to investigate the effects of surfactant on the drag and the shape of single bubbles rising through stagnant liquid. The predictions agreed well with the experimental data of Aoyama et al. (2016) and Chen et al. (2019) for the clean and fully-contaminated cases, respectively, and they proposed a shape correlation for bubbles in intermediately contaminated states as a function of the normalized drag coefficient. Atasi et al. (2018) carried out numerical simulations of contaminated bubbles in microchannels by using the level set method. Batchvarov et al. (2020) developed a hybrid method of the front-tracking and level set methods to investigate the dynamics of Taylor bubbles in microchannels. The hybrid method was also used for simulating the surfactant effects on the interface dynamics in bubble bursting at a free surface (Constante-Amores et al., 2021, 2022).

Although various studies have been carried out to understand the drag and the rise velocity of contaminated bubbles, the surfactant effect on the vorticity produced at the bubble interface and its impact on the drag have not been investigated in detail. In addition, to the authors' best knowledge, there is no comprehensive model of the stagnant-cap angle as a function of the ambient contamination state. In this study, effects of soluble surfactant on the vorticity produced at a spherical bubble in contaminated liquid were numerically investigated to make a complementary picture of the drag-vorticity relation under the influence of surfactant. Various combinations of independent dimensionless groups were considered to reproduce the different regimes of surface contamination and the dimensionless groups playing a key role in the drag and the interfacial vorticity of contaminated spherical bubbles were found. The dependence of the stagnant-cap angle on the relevant dimensionless groups was also discussed to develop a cap angle correlation, which would be of use when applying the stagnant-cap model.

2. Governing equations

A spherical bubble of the radius a fixed in a uniform flow of an incompressible Newtonian liquid at the velocity U is considered (Fig. 1; this problem is equivalent to a spherical bubble rising through stagnant liquid at U.) The continuity and Navier–Stokes equations nondimensionalized with the characteristic velocity and the length scales, U and d $(= 2a)$, are given by

$$\nabla \cdot \mathbf{u} = 0 \tag{1}$$

$$\frac{\partial \mathbf{u}}{\partial t} + \mathbf{u} \cdot \nabla \mathbf{u} = -\nabla p + \frac{\nabla^2 \mathbf{u}}{Re} \tag{2}$$

where $\mathbf{u}$ is the velocity, t the time, p the pressure, and Re the bubble Reynolds number defined by

$$Re = \frac{\rho_L U d}{\mu_L} \tag{3}$$

Here, ρ_L and μ_L are the liquid density and viscosity, respectively. The velocity component normal to the interface is zero, while the tangential velocity components of the liquid and the interface are the same. The momentum balance in the direction tangent to the interface is given by

$$\left(\mathbf{n} \cdot \nabla \mathbf{u} + Ma \nabla_S \sigma\right) \cdot \mathbf{t} = 0 \tag{4}$$

where $\mathbf{n}$ is the unit normal to the interface, $\mathbf{t}$ the unit tangential to the interface, ∇_S the surface gradient operator, and σ the surface tension, which is nondimensionalized with $R_G T \Gamma_{max}$, where R_G is the gas constant, T the temperature, and Γ_{max} the saturation value of the interfacial surfactant concentration. The Marangoni number, Ma, is defined by

$$Ma = \frac{R_G T \Gamma_{max}}{\mu_L U} \tag{5}$$

The transport equation of the concentration, C, of surfactant in the bulk liquid is given by

$$\frac{\partial C}{\partial t} + \nabla \cdot \mathbf{u} C = \frac{\nabla^2 C}{Pe} \tag{6}$$

where C is nondimensionalized with the bulk concentration, C_0, far from a bubble, and Pe the Péclet number defined by

$$Pe = \frac{U d}{D} \tag{7}$$

Here, D is the diffusion coefficient of surfactant in the liquid. The surfactant adsorbs to the interface and the interfacial surfactant concentration, Γ, normalized by Γ_{max} is governed by the following equation (Stone, 1990; Cuenot et al., 1997):

$$\frac{\partial \Gamma}{\partial t} + \nabla_S \cdot \mathbf{u} \Gamma = \frac{\nabla_S^2 \Gamma}{Pe_S} + \dot{S}_\Gamma \tag{8}$$

where Pe_S is the interface Péclet number defined by

$$Pe_S = \frac{U d}{D_S} \tag{9}$$

and D_S is the diffusion coefficient of surfactant at the interface. The $\mathbf{u}$ in the L.H.S. reduces to the interfacial velocity, $\mathbf{u}_S$, because of the velocity boundary condition. The adsorption–desorption flux, $\dot{S}_\Gamma$, of surfactant is evaluated using the following model for the Langmuir adsorption isotherm (Frumkin and Levich, 1947; Levich, 1962; Chang and Franses, 1995):

$$\dot{S}_\Gamma = Ha \left[C_S (1 - \Gamma) - \frac{\Gamma}{La} \right] \tag{10}$$

where C_S is the dimensionless bulk concentration at the interface. The Hatta number, Ha, for the adsorption flux and the Langmuir number, La, are defined by

$$Ha = \frac{k_a C_0 d}{U} \tag{11}$$

and

$$La = \frac{k_a C_0}{k_d} \tag{12}$$

respectively, where k_a is the adsorption rate constant, and k_d the desorption rate constant. The $\dot{S}_\Gamma$ balances with the diffusive flux at the interface, i.e.

$$-\mathbf{n} \cdot \nabla C = Pe K \dot{S}_\Gamma \tag{13}$$

where K is the dimensionless adsorption length defined by

$$K = \frac{\Gamma_{max}}{C_0 d} \tag{14}$$

The reduction in σ due to surfactant adsorption is given by the isotherm:

$$\sigma = \sigma_0 + \ln(1 - \Gamma) \tag{15}$$

where σ_0 is the dimensionless surface tension of surfactant-free interface.

We have thus introduced the dimensionless groups relevant to the problem. The Langmuir number is the ratio of the surfactant adsorption rate to the desorption rate. Therefore, when $La \ll 1$, the desorption is dominant and the contamination effect is weak. On the other hand, when $La \gg 1$, the adsorption is dominant and the bubble surface is expected to be highly contaminated. The Hatta number represents the ratio of the adsorption rate to the advection speed. A small Ha means that surfactant molecules adsorbing to the interface are immediately swept toward the rear of the bubble, which may result in a non-uniform profile of Γ along the interface (Hayashi and Tomiyama, 2012). The Marangoni number describes the competition between the magnitude of the viscous and Marangoni stresses at contaminated interfaces. The meaning of the dimensionless adsorption length K is briefly discussed in Appendix B.

3. Numerical condition

The numerical method proposed in Hayashi et al. (2022) was used in this study. Finite difference schemes were applied to discretize the governing equations as follows. The advection and diffusion terms of the Navier–Stokes and the surfactant transport equations were discretized using the Adams–Bashforth and Crank–Nicolson schemes, respectively. The second-order ENO (essentially non-oscillatory) (Shu and Osher, 1989) and the second-order centered difference schemes were used for spatial differentiation of the advection and diffusion terms, respectively. The fractional-step method (Choi and Moin, 1994) was used for velocity-pressure coupling. The present method was validated in our previous paper (Hayashi et al., 2022) by comparing the numerical results of spherical bubbles and drops in contaminated systems with numerical (Cuenot et al., 1997) and experimental data (Hosokawa et al., 2017), respectively. See Hayashi et al. (2022) for more details.

It was assumed that the flow about a bubble was axisymmetric and the bubble shape was imposed to be spherical. The two-dimensional spherical coordinates, (r, θ), were used. The center of the bubble was located at the origin of the coordinates, so that the bubble interface was given by $r = a$. The computational domain was also spherical, and its radius was $80a$, which is the same as used in Cuenot et al. (1997). The drag force F_D and the drag coefficient C_D were calculated as follows:

$$F_D = 2\pi a^2 \int_0^\pi \left\{ p \cos\theta - \frac{2}{Re} \frac{\partial u_r}{\partial r} \cos\theta + \frac{1}{Re} \left(\frac{\partial u_\theta}{\partial r} - \frac{u_\theta}{r} \right) \sin\theta \right\}_{r=a} \sin\theta d\theta \tag{16}$$

$$C_D = \frac{F_D}{\frac{1}{2} \rho_L U^2 \pi a^2} \tag{17}$$

where u_r and u_θ are the r and θ components of $\mathbf{u}$, respectively.

The number of computational cells in the r and θ directions were 50 and 60, respectively. The grid spacing in the θ direction was uniform, while non-uniform spacing was used for the r direction so as to capture the boundary layer in the vicinity of the interface (Cuenot et al., 1997). Blanco and Magnaudet (1995) reported that two grid points within the momentum boundary layer are sufficient to accurately predict drag coefficients. Cuenot et al. (1997) used three grid

points within the concentration boundary layer to resolve the gradient of the surfactant concentration. The latter condition was employed in the present study. Grid dependence was tested for clean bubbles and solid spheres at $Re = 1$ and 100 as limiting cases. The numbers of the computational cells were varied as 50, 75, 100, 125 and 60, 80, 100, 120 for the r and θ directions, respectively. The change in the spatial resolution gave a difference in C_D at most 0.5%. All the results given in this study are the steady state solutions. It should be noted that in the steady state the global mass transfer rate at the bubble interface is zero (Cuenot et al., 1997) whereas the local interfacial flux is non-zero as will be shown later (Fig. 4(j)–(l)).

In the present study, the different surface contamination regimes are considered over a wide range of Langmuir La, Marangoni Ma and Hatta Ha numbers in both the diffusion-dominant case and advection-dominant case, $Re = Pe = 1$ and $Re = Pe = 100$, respectively, so that the Schmidt numbers were unity in both cases. The diffusion coefficient at the interface has often been assumed to be the same as the bulk diffusion coefficient, i.e., $Pe = Pe_S$. We also used this assumption in the present simulations. In the case of $Re = 100$, the following ranges of La, Ma and Ha were used: $0.001 \le La \le 10$, $0.1 \le Ma \le 10\,000$, and $0.0002 \le Ha \le 10$. The ranges of the dimensionless groups used in the case of $Re = 1$ were $0.1 \le La \le 10$, $0.1 \le Ma \le 50$, and $0.001 \le Ha \le 10$. Typical values of the dimensionless groups for decanoic acid, Triton X-100 and 1-pentanol are given in Appendix A. In Sections 4.3 and 4.4, the dimensionless adsorption length $K = 1$ was used. This is the typical value for decanoic acid (Cuenot et al., 1997). The choice of K was found to have no impact on the result by varying its value from 0.1 to 10 (see Appendix B).

In real systems, bubbles are usually spherical for the Reynolds numbers Re considered here but the Péclet number Pe would be larger. Cuenot et al. (1997) used $Pe = 10^5$ much larger than the present one. The diffusion coefficient of surfactant is typically 10^{-9} m^2/s, so that the typical value of Pe can be 10^5. The high Pe requires very thin computational mesh in the vicinity of the interface to resolve the thin concentration boundary layer (Cuenot et al., 1997; Hayashi et al., 2022). However, Fukuta et al. (2008) carried out numerical simulations of a spherical bubble at $Re = 100$ and pointed out that a drastic reduction in Pe from 10^5 to 100 does not have a significant impact on the drag and lift forces. Takagi et al. (2003) also obtained very good agreement between predicted and measured drag coefficients of spherical bubbles at intermediate surfactant concentrations with the reduced Péclet number, $Pe = Pe_S = 100$. Fig. D.21 in Appendix D shows that considering $Pe = 100$ instead of $Pe = 10^5$, in other words the bulk Schmidt number, does not impact the result so much in term of the surface vorticity distribution, in particular for the stagnant-cap (IS-c) regime specific of the high interfacial Péclet number condition. Hence, the numerical condition of $Pe = 100$ was selected since it enables us to reduce the numerical cost without losing the important physics in the dynamics of contaminated bubbles in the actual systems. Indeed, the objective here is not to exactly replicate some given experiments, but to solve the theoretical system of equation and provide accurate solutions by reproducing the four different regimes of interface contamination introduced above, namely (IS-a), (IS-b), (IS-c) and (IS-d). What discussed here is the relation of the surface contamination with the drag force via the description of the vorticity produced at the bubble interface. The connection then helps to relate the drag to the dimensionless groups used for the characterization of the contamination mechanisms.

4. Results and discussion

4.1. Drag-vorticity relation for clean bubble and solid sphere

The main objective of this work is to investigate how the vorticity distribution on the interface of a contaminated bubble impacts its drag coefficient. Let us first discuss the drag-vorticity relations for clean spherical bubbles and solid spheres as limiting cases of contaminated bubbles. The vorticity produced at the bubble interface has been shown to play an important role in the bubble dynamics (Legendre, 2007; Stone, 1993; Hidman et al., 2022). The drag force acting on a body moving steadily in an inviscid incompressible flow is given by the vortex force, i.e., $\int_V \rho \mathbf{u} \times \boldsymbol{\omega} dV$ (Saffman, 1992), where $\boldsymbol{\omega}$ is the vorticity vector, and ρ and V are the density and the volume of the surrounding fluid, respectively. The vorticity produced at the interface of the body is the only vorticity source in the system. Therefore, in particular a condition of zero interfacial vorticity results in a zero drag force so that the magnitude of maximum interfacial vorticity, ω_{max}, is a good marker of the magnitude of the drag force.

Legendre (2007) derived the following drag-vorticity relation for clean spherical bubbles in viscous liquid by scaling the Hadamard–Rybczynski drag (Hadamard, 1911; Rybczynski, 1911) with the maximum interfacial vorticity:

$$C_D = \frac{16}{Re}\omega^B_{max} \tag{18}$$

where the vorticity is nondimensionalized with U and a, and the superscript B denotes clean bubble. $\omega^B_{max} \to 1$ as $Re \to 0$ and $\omega^B_{max} \to 3$ as $Re \to \infty$ (Magnaudet and Mougin, 2007). Hence, Eq. (18) reduces to the Hadamard–Rybczynski drag, $C_D = 16/Re$, and to the Levich drag, $C_D = 48/Re$ (Levich, 1962), for $Re \ll 1$ and $Re \to \infty$, respectively. Legendre (2007) carried out numerical simulations of clean spherical bubbles at various Re and showed that Eq. (18) is valid not only in the limiting cases, but also for finite Re in-between the limiting cases as shown in Fig. 2(a). As demonstrated in the embedded sub-figure, the predictions of C_D agree well with the following correlation proposed by (Mei et al., 1994):

$$C_D = \frac{16}{Re}\left(\frac{16 + 3.315\sqrt{Re} + 3Re}{16 + 3.315\sqrt{Re} + Re}\right) \tag{19}$$

and therefore, combining Eqs. (18) and (19) yields (Legendre, 2007)

$$\omega^B_{max} = \frac{16 + 3.315\sqrt{Re} + 3Re}{16 + 3.315\sqrt{Re} + Re} \tag{20}$$

For solid spheres in the Stokes regime, the maximum interfacial vorticity is given by $\omega^S_{max} = 3/2$ and Eq. (18) holds (Legendre, 2007), i.e., $C_D = 24/Re$, where the superscript S denotes solid sphere. The ω^S_{max} increases as Re increases. By making use of the drag correlation proposed by (Schiller and Naumann, 1933)

$$C_D = \frac{24}{Re}(1 + \Phi(Re)) \tag{21}$$

we may write

$$\omega^S_{max} = \frac{3}{2}(1 + \Phi(Re)) \tag{22}$$

where

$$\Phi(Re) = 0.15Re^{0.687} \tag{23}$$

and a comparison between the correlation and predicted C_D is shown in the sub-figure of Fig. 2(a). This expression of ω^S_{max} is valid only with a weak inertial effect (up to $Re \sim 1$) and deviates from predictions as ω^S_{max} increases as shown in Fig. 2 although the inertial-effect multiplier, $\Phi(Re)$, provides a good description of the drag force up to $Re \sim 800$. The drag-vorticity relation, Eq. (18), is therefore no longer valid for solid spheres for $Re > 1$. However, the following linear relation well expresses the data:

$$C_D Re = 11\omega^S_{max} + 7.5 \tag{24}$$

Substituting Eq. (21) into C_D of this relation yields

$$\omega^S_{max} = \frac{3}{2} + \frac{24\Phi(Re)}{11} \tag{25}$$

The first term in the R.H.S. of Eq. (25) is ω^S_{max} for $Re \to 0$ and the second term represents the inertial effect on the vorticity. The trend of ω^S_{max} largely different from that of ω^B_{max} is attributed to the fact that the breakdown of the fore-aft symmetry in the vorticity profile at the solid

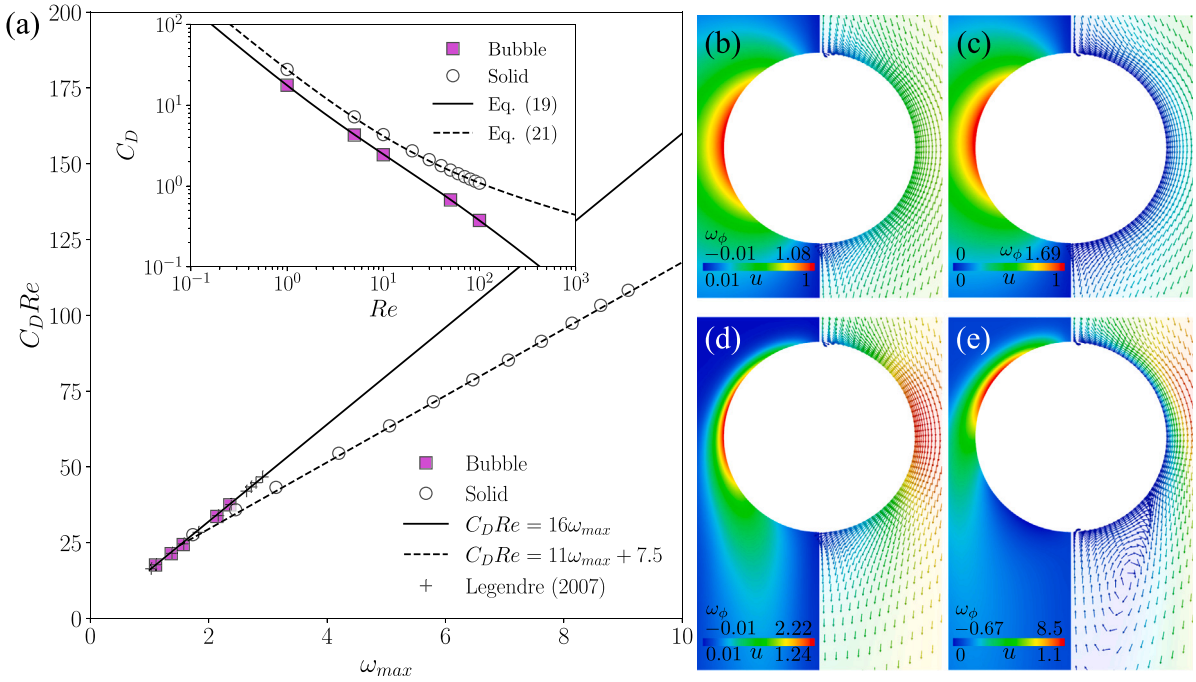

Fig. 2. (a) $C_D Re$ of clean bubbles and solid spheres. The sub-figure shows drag coefficients of spherical bubbles and solid spheres. The Reynolds number of the present numerical data of bubbles and solid spheres ranges from 1 to 100. (b) Bubble of $Re = 1$, (c) Solid sphere of $Re = 1$, (d) Bubble of $Re = 100$, (e) Solid sphere of $Re = 100$ (the left and right panels are ω_ϕ and **u**, respectively, and the color map is adjusted for the maximum and minimum values in each case.). (For interpretation of the references to color in this figure legend, the reader is referred to the web version of this article.)

surface with increasing Re is more remarkable than that at the bubble interface and especially a separation of flow takes place in the solid sphere cases (Fig. 2(b)–(e)). See Appendix C for a slight modification of Eq. (24) for small Re cases.

4.2. Typical distributions of interfacial vorticity

Typical vorticity distributions corresponding to the different surface contamination regimes are reported in Fig. 3, where ω_ϕ is the azimuthal component of interfacial vorticity normalized using U and a, and defined by

$$\omega_\phi = \frac{1}{2}\frac{\partial u_\theta}{\partial r} + u_\theta \tag{26}$$

Here, ω_ϕ is nondimensionalized with a and U. The balance between the tangential viscous stress and the Marangoni stress (the boundary condition of Eq. (4)) can be written as

$$\frac{1}{2}\frac{\partial u_\theta}{\partial r} - u_\theta = -Ma\frac{\partial \sigma}{\partial \theta} \tag{27}$$

Combining this equation and Eq. (26) and using the isotherm (Eq. (15)) yield (Atasi et al., 2023)

$$\omega_\phi = 2u_\theta + \frac{Ma}{1-\Gamma}\frac{\partial \Gamma}{\partial \theta} \tag{28}$$

We recover $\omega_\phi = 2u_\theta$ for a clean interface, and the surface vorticity increases with the increase in the surface surfactant concentration Γ and its gradient.

As shown by Fig. 3, depending on the bubble surface contamination different vorticity distributions are observed when reported as a function of θ, the angle measured from the bubble nose. For the advection-dominant case ($Re = Pe = 100$), Fig. 3(a) shows ω_ϕ distributions typically observed for the surface contamination. The ω_ϕ distribution at $(Ma, La, Ha) = (50, 0.001, 0.002)$ (the circular symbols) is close to that of a clean bubble, the (IS-a) fully mobile surface regime, although a slight increase in the vorticity takes place in the rear part of the bubble. The maximum vorticity is therefore almost the same as that of the clean bubble. The slight contamination effect is due to the small La. The vorticity distribution in the liquid phase shown in Fig. 3(c) (left) is also similar to that of clean bubble (Fig. 2(d)). Increasing Ma and La as illustrated here at 70 and 0.02, respectively, yields a larger Marangoni stress, resulting in the stagnant-cap (IS-c) regime with a remarkable peak in ω_ϕ (the triangles). As can be understood from Eq. (28), the formation of the peak is the result of a steep Γ gradient (see also Fig. 12(d) and (g)). The vorticity in the rear of the bubble agrees with that of a solid sphere, while in the front half of the bubble the ω_ϕ profile is similar to that of the clean bubble. The negative value of ω_ϕ in the rear is due to a separation of the flow. In the ω_ϕ distribution at $(Ma, La, Ma) = (20, 0.2, 0.001)$, also the (IS-c) stagnant cap regime, a peak also appears, while the region behaving like the solid sphere is wider compared with the smaller La case. Note that the peak values tend to exceed ω^S_{max}. High ω_ϕ regions are observed in the liquid phase around the ω_ϕ peaks (Fig. 3(d)). The presence of the peaks is the typical signature of the (IS-c) stagnant-cap state. In the case of $(Ma, La, Ha) = (500, 0.12, 6)$, the large Ha allows the surfactant to accumulate at the interface at a high concentration level, and the large Ma causes a large Marangoni stress, which makes the interface almost immobile, corresponding to the fully immobile surface (IS-d) regime. The ω_ϕ distribution is thus similar to that of the solid sphere; the vorticity distribution in the liquid phase (Fig. 3(c) (right)) is comparable to that of solid sphere (Fig. 2(e)).

Fig. 3(b) and (e) show the ω_ϕ distributions for the diffusion-dominant case ($Re = Pe = 1$), for which the diffusion of surfactant plays a dominant role in the vorticity profile. The bubble with weak contamination (the circular symbols) has the ω_ϕ distribution similar to that of clean bubble, the (IS-a) fully mobile surface regime. The largely contaminated bubble shows ω_ϕ (the square symbols) close to ω^S_ϕ and corresponds to the fully immobile surface (IS-d) regime. However, even at intermediately contaminated conditions, ω_ϕ (the cross symbols) does not have spikes in its profile because of the strong diffusion, i.e., thus corresponding to the uniformly retarded surface mobility (IS-b) regime.

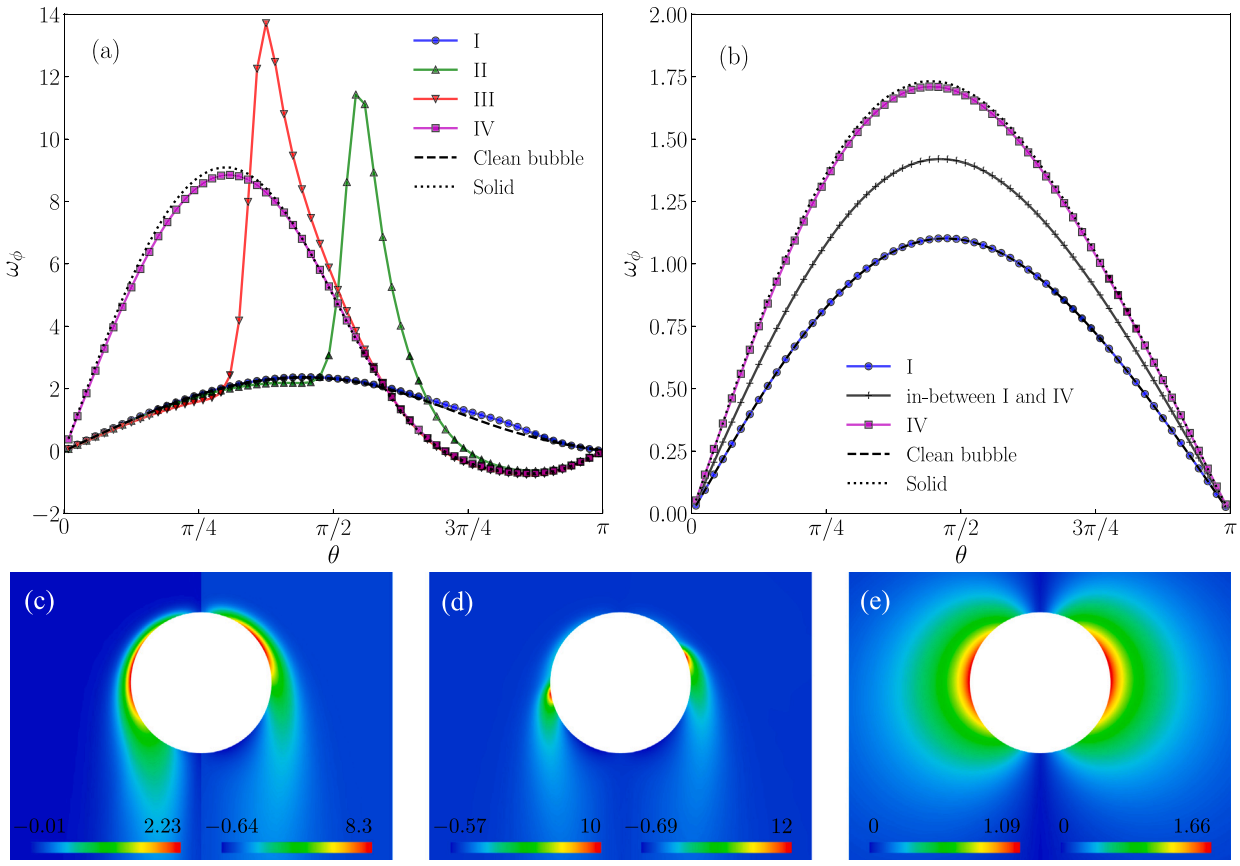

Fig. 3. Typical ω_ϕ distributions for the different surface contamination regimes. (a) Advection-dominant case ($Re = Pe = 100$): $(Ma, La, Ha) = (50, 0.001, 0.002)$ resulting in the (IS-a) surface regime and the drag regime I, $(70, 0.02, 0.002)$ resulting in the (IS-c) surface regime and the drag regime II, $(20, 0.2, 0.001)$ resulting in the (IS-c) surface regime and the drag regime III, $(500, 0.12, 6)$ resulting in the (IS-d) surface regime and the drag regime IV ; (b) Diffusion-dominant case ($Re = Pe = 1$): $(Ma, La, Ha) = (0.1, 0.1, 0.001)$ resulting in the (IS-a) surface regime and the drag regime I, $(20, 10, 1)$ resulting in the (IS-d) surface regime and the drag regime IV, $(30, 0.5, 5)$ resulting in the (IS-b) surface regime and a drag regime in between I and IV. (c) ω_ϕ distributions in liquid phase at $Re = 100$ (Regime I (left) and Regime IV (right)), (d) Regime II (left) and Regime III (right) at $Re = 100$, (e) Regime I (left) and IV (right) at $Re = 1$.

Note that due to the surfactant diffusion along the interface the (IS-c) stagnant cap regime is not observed.

As it will be detailed in the following, a specific impact of the surface contamination on the vorticity produced at the interface and thus on the drag force was found in each regime. In particular, four different Regimes on how the drag/surface vorticity depends on the surface contamination, namely I, II, III and IV, will be identified:

- Regime I: the drag and the vorticity show linear dependence on the dimensionless group Π_M $(= LaMa)$ which will be defined later in Eq. (40),
- Regimes II and III: the relationships between the drag/the vorticity and Π_M become more complex, while non-linear relationships will be found for each regime,
- Regime IV: the large contamination effect leads to an inversely proportional relationship between the drag/the vorticity and Π_M,

.

The diffusion-dominant case is simpler than the advection-dominant case and will be discussed first in Section 4.3. The drag-vorticity relation in the advection-dominant case will then be presented in Section 4.4.

4.3. Diffusion-dominant case ($Re = Pe = Pe_S = 1$)

Fig. 4(a) shows the tangential surface velocity u_θ at $La = 0.1$ and $Ha = 0.002$. The solid line represents u_θ of a clean bubble. The increase in Ma, i.e., the increase in the Marangoni effect, deteriorates the surface mobility, so that the magnitude of u_θ decreases. The maximum value of u_θ appears at $\theta = 0.471\pi$, which is slightly less than $\theta = \pi/2$ due to the presence of small inertial effects at such Re. The contamination shifts the angle for the maximum u_θ toward the front side, i.e., $\theta =$ 0.462 π, 0.455 π and 0.446 π for $Ma = 10$, 20 and 40, respectively. This trend is clearer in more contaminated cases ($La = 1$) as shown in Fig. 4(b). The magnitude of u_θ at $La = 10$ shown in Fig. 4(c) are much smaller than that of the clean bubble; however the values are still non-zero.

Fig. 4(d) shows the surfactant concentration Γ at $La = 0.1$. Ha is very small in this condition, which means the adsorption rate is much smaller than the advection velocity and the surfactant tends to be swept toward the rear of the bubble. However, the surfactant diffusion is strong since $Pe_S = 1$, so that the concentration of surfactant accumulated on the interface can take non zero values even at the bubble front $\theta = 0$, i.e. $\Gamma = 0.07$. The effect of Ma on Γ is small. The increase in La allows surfactant molecules to adsorb more to the interface, so that Γ increases with increasing La as shown in Fig. 4(e). The effect of Ma becomes somewhat visible with larger La. However, further increase in La hinders the effect of Ma on Γ since Γ approaches the saturation value. For the adsorption–desorption equilibrium in the absence of any fluid flow, the equilibrium concentration of surfactant on the interface is given by

$$\Gamma_{eq} = \frac{La}{La + 1} \tag{29}$$

This equation gives $\Gamma_{eq} = 0.091$, 0.5 and 0.91 for $La = 0.1$, 1 and 10, respectively. These values agree well with the numerical predictions of Γ at $\theta = \pi/2$, i.e. $\Gamma|_{\theta=\pi/2} = 0.0905$, 0.50 and 0.89, respectively.

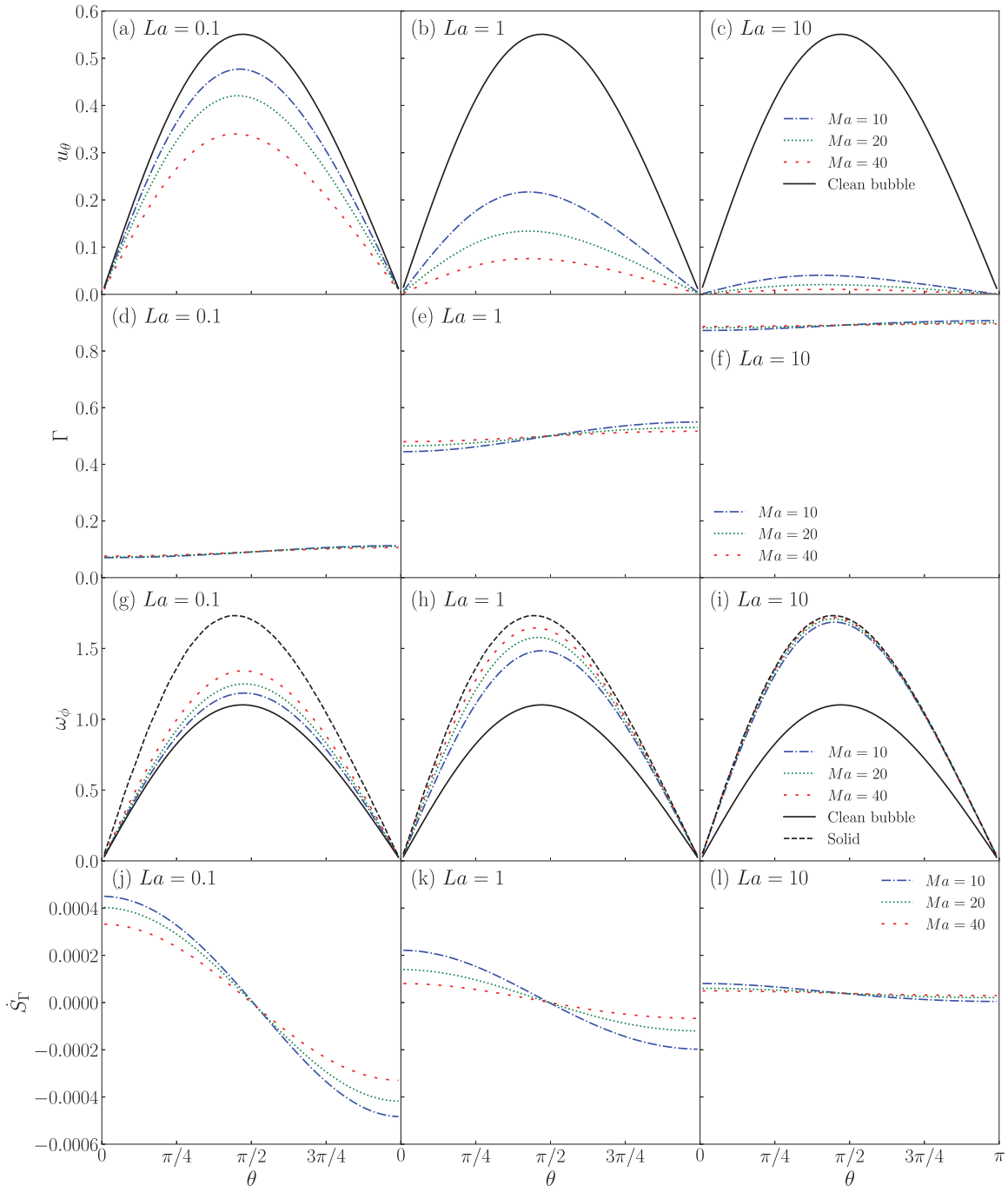

Fig. 4. Interface profiles of the tangential velocity u_θ, the surfactant concentration Γ, the interfacial vorticity ω_ϕ, and the adsorption–desorption flux $\dot{S}_\Gamma$ at $Ha = 0.002$ in the diffusion-dominant case ($Re = Pe = Pe_S = 1$).

The interfacial vorticity ω_ϕ of the contaminated bubbles are in the range from ω_ϕ^B to ω_ϕ^S as shown in Fig. 4(g)–(i). The increase in La and Ma increases ω_ϕ and the value of ω_ϕ approaches ω_ϕ^S. This dependence will be derived from Eq. (28) in the following discussion. Fig. 5 shows the dimensionless combination $C_D Re$ of contaminated bubbles plotted against the maximum value of the surface vorticity ω_{max}. The increase in ω_{max} increases $C_D Re$ and these clearly show a remarkable linear relation expressed by Eq. (18) ($C_D Re = 16\omega_{max}$). The contaminated bubble data become slightly lower than the solid line as ω_{max} increases, which implies that inertial effects provide a second order correction to the drag-vorticity relation. Thus, the effects of La, Ma and Ha on C_D can be accounted for via ω_{max} by expressing ω_{max} in terms of the relevant dimensionless groups.

The adsorption–desorption flux $\dot{S}_\Gamma$ is shown in Fig. 4(j). As already mentioned, $\dot{S}_\Gamma$ takes non-zero values depending on θ though the net flux for the whole interface is zero (Cuenot et al., 1997). The fluxes exhibit cosinusoidal curves as predicted in the analysis of Levich (1962) for the Stokes regime; their value is positive (adsorption dominant) in the front half of the bubble while becomes negative (desorption dominant) in the rear half. The increases in Ma and La decrease the magnitude of the flux curve as shown in Fig. 4(j)–(l). This is due to the fact that both Ma and La deteriorate the surface mobility, so that $\dot{S}_\Gamma$

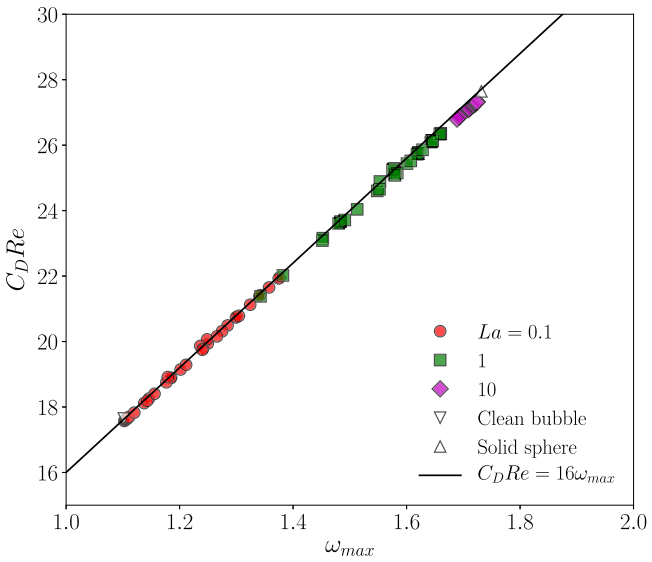

Fig. 5. $C_D Re$ of contaminated bubbles plotted against ω_{max} ($Re = Pe = Pe_S = 1$).

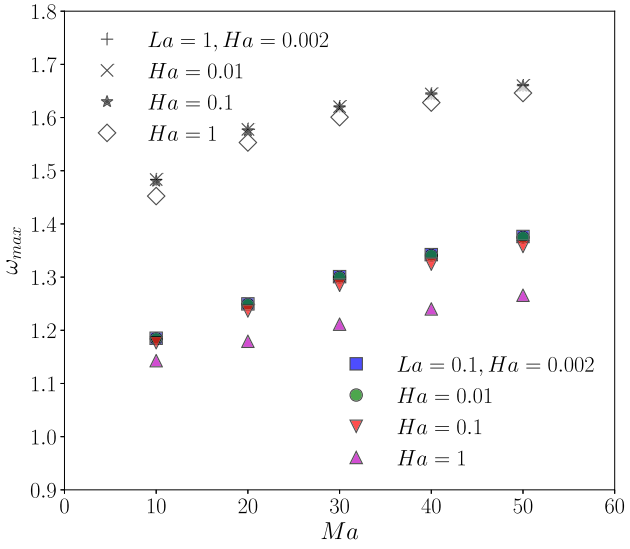

Fig. 6. Effects of La, Ma and Ha on ω_{max} ($Re = Pe = Pe_S = 1$).

approaches zero for immobile interface with $\Gamma = \Gamma_{eq}$. In these cases, the dimensionless bulk concentration of surfactant at interface is $C_S \sim 1$.

Fig. 6 shows effects of La, Ma and Ha on ω_{max}, which increases with the increase in La and Ma. On the other hand, Ha rarely affects ω_{max} when $Ha/La < 1$, where the dimensionless group (Fukuta et al., 2008)

$$\Pi_H = \frac{Ha}{La} \left(= \frac{k_d d}{U} \right) \tag{30}$$

can be regarded as the Hatta number for the desorption rate and appears in the adsorption–desorption flux, Eq. (10):

$$\dot{S}_\Gamma = \Pi_H \left[La C_S (1 - \Gamma) - \Gamma \right] \tag{31}$$

The increase in Ha decreases ω_{max}, meaning that the increase (decrease) in the adsorption rate (interfacial velocity) mitigates the gradient of the interfacial surfactant concentration. In the limiting case of $\Pi_H \to \infty$, the effect of the interfacial advection disappears, resulting in no Marangoni effect, i.e. $\omega_{max} = \omega^B_{max}$. Let us first consider the effects of La and Ma on ω_{max} in the small Π_H range.

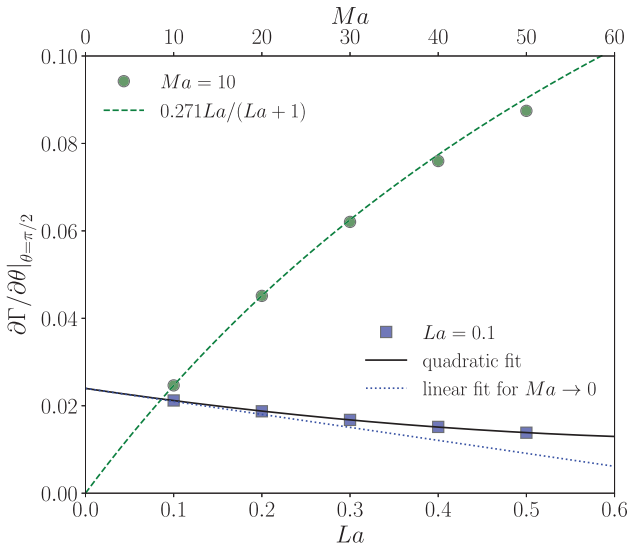

Fig. 7. $\partial\Gamma/\partial\theta|_{\theta=\pi/2}$ plotted as a function of La (circles) and Ma (squares) for $Ha = 0.002$ ($Re = Pe = Pe_S = 1$).

For simplicity let us consider the limiting case of $Re \to 0$. For a surfactant free interface, the second term of Eq. (28) disappears and $u_\theta|_{\theta=\pi/2} = 1/2$. Thus, $\omega_{max} = \omega^B_{max} = 1$. The role of La and Ma at weakly contaminated interfaces is then discussed. In the limiting case of $Re \to 0$ for a clean interface, the maximum value of u_θ (and ω_ϕ) occurs at $\theta = \pi/2$ (the Hadamard–Rybczynski solution). Furthermore, for contaminated interfaces, we expect maximum values of u_θ and ω_ϕ at $\theta = \pi/2$, provided that diffusion is dominant in interfacial surfactant transport, yielding a symmetric concentration distribution. The order of Γ at $\theta \sim \pi/2$ can be estimated as

$$\Gamma|_{\theta=\pi/2} \sim \Gamma_{eq} \tag{32}$$

Substituting Eq. (32) into Eq. (28) and considering Eq. (29) yield

$$\omega_\phi\Big|_{\theta=\pi/2} \sim 2\, u_\theta|_{\theta=\pi/2} + (La+1) Ma \left.\frac{\partial\Gamma}{\partial\theta}\right|_{\theta=\pi/2} \tag{33}$$

Fig. 7 shows $\partial\Gamma/\partial\theta|_{\theta=\pi/2}$ at small La, where $Ma = 10$ and $Ha = 0.002$. The gradient of Γ at low La is small since the amount of surfactant adsorbing to the interface is small. It increases with increasing La and is well scaled by Γ_{eq}. The dependence of Γ gradient on Ma at $La = 0.1$ is also shown in the figure. The effect of Ma on the Γ gradient is much weaker than that of La in the present ranges of La and Ma. Hence,

$$\left.\frac{\partial\Gamma}{\partial\theta}\right|_{\theta=\pi/2} \sim \frac{c_g La}{La+1} \tag{34}$$

where c_g is a coefficient and the Ma dependence is neglected. With this expression, Eq. (33) becomes

$$\omega_\phi\Big|_{\theta=\pi/2} \sim 2\, u_\theta|_{\theta=\pi/2} + c_g LaMa \tag{35}$$

Fig. 8 shows that ω_{max} is proportional to $LaMa$ for weak contamination as predicted by Eq. (35), and this defines Regime I observed at low contamination level. The coefficients in the linear fit for the small $LaMa$ range can be represented by using ω^B_{max} and ω^S_{max}, i.e.,

$$\omega_{max} \approx \omega^B_{max} + \left(\omega^S_{max} - \omega^B_{max}\right) c_w LaMa \tag{36}$$

where $c_w = 1/7.0$. The exceed of vorticity is related to the parameter, $LaMa$, controlling the interface contamination.

At large contamination level, ω_{max} can also be correlated in terms of $LaMa$ as follows. For a fully-contaminated interface, $\omega_{max} = \omega^S_{max} = 3/2$ and $u_\theta = 0$, and therefore,

$$\left.\frac{\partial\Gamma}{\partial\theta}\right|_{\theta=\pi/2} = \frac{3(1 - \Gamma|_{\theta=\pi/2})}{2Ma} \tag{37}$$

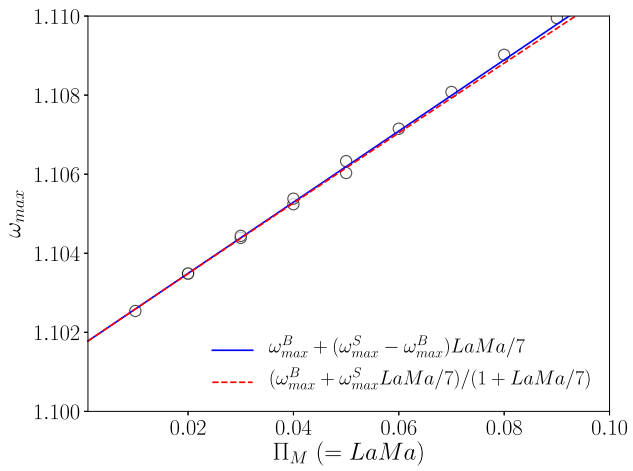

Fig. 8. ω_{max} for small $\Pi_M = LaMa$. The dashed line is a linear fit to the data. ($Re = Pe = Pe_S = 1$).

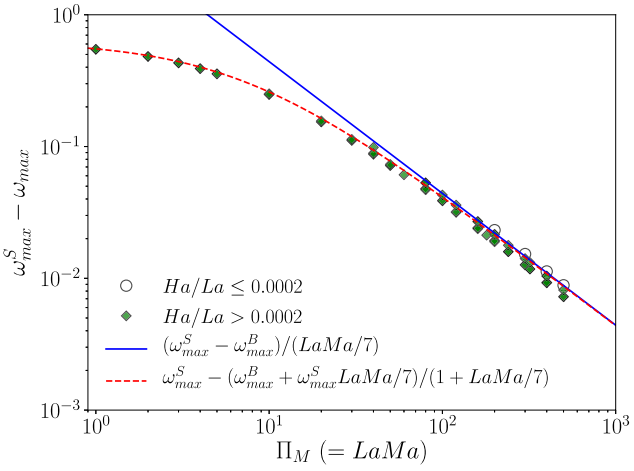

Fig. 9. $\omega^S_{max} - \omega_{max}$ as a function of $\Pi_M = LaMa$. The fitting equation is given by Eq. (39). ($Re = Pe = Pe_S = 1$).

Substituting Eq. (32) into Eq. (37) yields

$$\left.\frac{\partial \Gamma}{\partial \theta}\right|_{\theta=\pi/2} \sim \frac{3}{2Ma(La+1)} \tag{38}$$

The gradient of Γ becomes small with increasing Ma and La but is still non zero so as to satisfy $Ma(1-\Gamma)^{-1}\partial\Gamma/\partial\theta \to \omega^S_{max}$ for the limiting case of $Ma, La \to \infty$. Therefore, the behavior of the gradient of Γ must change from Eqs. (34) to (38). The factor required for this modification is $(LaMa)^{-1}$. Fig. 9 shows $\omega^S_{max} - \omega_{max}$ to demonstrate the behavior of ω_{max} at large values of $LaMa$ in detail. The data are nearly proportional to $(LaMa)^{-1}$ at large $LaMa$ as expected, and therefore,

$$\omega_{max} \approx \omega^S_{max} - \frac{\omega^S_{max} - \omega^B_{max}}{c_w LaMa} \tag{39}$$

This defines Regime IV observed at high level of contamination. Here the deficit of vorticity compared to the fully-contaminated bubble is expressed in term of $LaMa$. The reason of the difference in the dependence of ω_{max} on $LaMa$ in these limiting cases can be understood as follows: a clean interface is free to welcome surfactant, while in a contaminated situation it requires large values of $LaMa$ to reach the fully-contaminated condition.

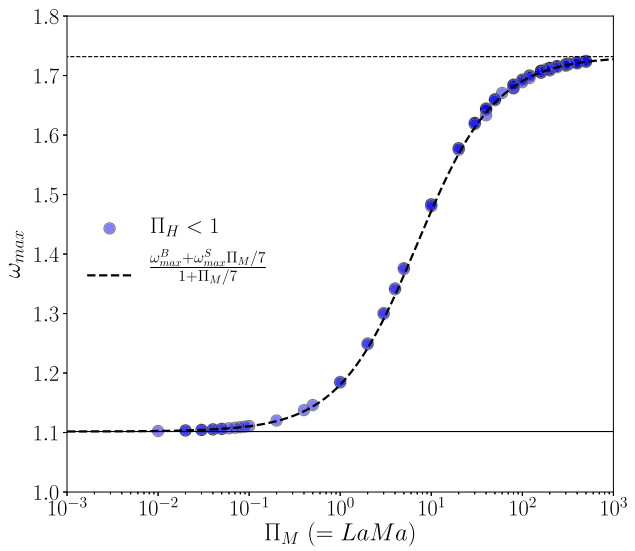

Fig. 10. Comparison between predicted ω_{max} and Eq. (41). The lower and upper horizontal lines represent ω^B_{max} and ω^S_{max}. ($Re = Pe = Pe_S = 1$).

It has been revealed that ω_{max} in the limiting cases can be simply expressed in terms of the dimensionless group

$$\Pi_M = LaMa \left(= \frac{k_a C_0}{k_d} \cdot \frac{R_G T \Gamma_{max}}{\mu_L U}\right) \tag{40}$$

and it is interesting that La and Ma, which appear in the adsorption–desorption flux and in the momentum balance at the interface, respectively, contribute to the increase in ω_{max} with the same power. The following weighting average reduces to Eq. (36) when $\Pi_M \to 0$ and to Eq. (39) when $\Pi_M \to \infty$:

$$\omega_{max} = \frac{\omega^B_{max} + \omega^S_{max} c_w \Pi_M}{1 + c_w \Pi_M} \tag{41}$$

Fig. 10 shows the effects of Π_M on ω_{max} and the data are compared with Eq. (41). The correlation expresses the effects of the dimensionless groups well not only for Regimes I and IV, but also for the intermediate regime (in-between I and IV), provided that Π_H is small, i.e., the desorption is slower than the interfacial advection.

Let us assume that the effects of Ha on ω_{max} can be accounted for in the following form:

$$\omega_{max} = \frac{\omega^B_{max} + \omega^S_{max} \frac{c_w \Pi_M}{(1+\Psi)}}{1 + \frac{c_w \Pi_M}{(1+\Psi)}} \tag{42}$$

The values of Ψ were evaluated using the numerical predictions and fitting to the predicted data yielded

$$\Psi(\Pi_H, La) = (0.03La + 0.115)\Pi_H \tag{43}$$

Fig. 11 shows comparisons of ω_{max} between the predictions and Eq. (42), in which the effect of Π_H is accounted for. The factor $\Psi(\Pi_H, La)$ works to reproduce the effect of Ha on the vorticity. Thus, C_D can be written as

$$C_D = \frac{16}{Re}\omega_{max} = \frac{16}{Re}\left[\frac{\omega^B_{max} + \omega^S_{max}\frac{c_w\Pi_M}{1+\Psi}}{1 + \frac{c_w\Pi_M}{1+\Psi}}\right] \tag{44}$$

A bubble behaves like a clean bubble when $\Pi_M \ll 1$, while the interface is immobile when $\Pi_M \gg 1$. As shown in Fig. 4(d)–(f), the Langmuir number controls the mean surfactant concentration (the contamination level), which is close to Γ_{eq}. The Marangoni number represents the ease with which the bubble interface is immobilized by the Marangoni

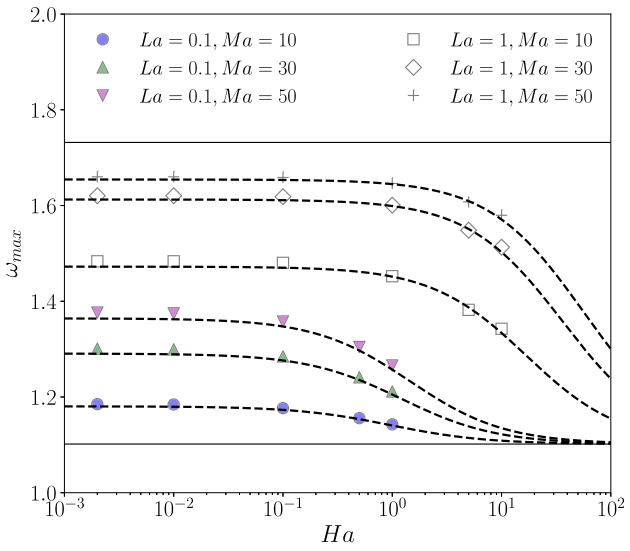

Fig. 11. Comparison between predicted ω_{max} and Eq. (42) (the dashed lines). The lower and upper solid lines represent ω^B_{max} and ω^S_{max}, respectively. ($Re = Pe = Pe_S = 1$).

stress; a low-viscosity liquid requires a large velocity gradient at the interface to balance with the Marangoni stress proportional to the factor $R_G T \Gamma_{max}$, in other words, the interface mobility tends to easily deteriorate in systems with low viscosity or large Γ_{max}. The interface immobilization takes place if the Langmuir number is large enough even with small Marangoni number, and vice versa. Thus, Π_M represents the degree of contamination effect on the drag and vorticity. The parameter Π_H represents how fast surfactant can desorb from the interface while traveling from the bubble nose to rear. When $\Pi_H \to 0$, desorption does not affect the Γ profile, and therefore Π_H does not play a role in drag and vorticity. For finite values of Π_H, we need to introduce not only the desorption property (Π_H) but also the adsorption property (Ha) in the vorticity equation as shown in Eq. (43), $\Psi(\Pi_H, La) = (0.03La + 0.115)\Pi_H = 0.03Ha + 0.115\Pi_H$.

The normalized drag coefficient (Cuenot et al., 1997)

$$\xi = \frac{C_D - C_D^B}{C_D^S - C_D^B} \tag{45}$$

is known to be strongly related with the stagnant-cap angle, θ_{cap}. Though the bubbles of $Re = Pe = 1$ are not in the stagnant-cap state, expressing the drag coefficient in the form of $C_D = 16\omega_{max}/Re$ yields

$$\xi = \frac{\omega_{max} - \omega^B_{max}}{\omega^S_{max} - \omega^B_{max}} \tag{46}$$

Hence, Eq. (42) can also be written in the normalized drag form as follows:

$$\xi = \frac{1}{1 + \frac{1+\Psi}{c_w \Pi_M}} \tag{47}$$

For the limiting cases of $\Pi_M \to 0$ and $\Pi_M \to \infty$, $\xi = c_w\Pi_M/(1+\Psi)$ and $\xi = 1 - (1+\Psi)/c_w\Pi_M$, respectively. Furthermore, when $\Pi_H \to 0$,

$$\xi = \begin{cases} c_w \Pi_M & \text{(Regime I)} \\ 1 - (c_w \Pi_M)^{-1} & \text{(Regime IV)} \end{cases} \tag{48}$$

Let us now define Regimes I and IV more precisely as follows: Regime I is the regime in which ξ is proportional to Π_M, and Regime IV is the regime in which ξ is inversely proportional to Π_M. Regime I and Regime IV are the asymptotic limits for regular distribution of vorticity at the interface in the diffusion-dominant situations, for low and high level of contamination, respectively.

4.4. Advection-dominant case ($Re = Pe = P_S = 100$)

The tangential velocities u_θ of contaminated bubbles at $La = 0.1$ and $Ha = 0.01$ are shown in Fig. 12(a). The velocity profile at small θ agrees with that of the clean bubble, while a steep decrease in u_θ takes place at a certain θ and $u_\theta \sim 0$ for larger θ. The fore-aft symmetry observed in the clean bubble case disappears in the contaminated cases. Fig. 12(d) shows that the surfactant concentration Γ in the small θ region is very small and θ for the steep decrease of u_θ corresponds to that of relatively large Γ gradient. The bubble surface is in the stagnant cap state (IS-c), for which Cuenot et al. (1997) gave a description of the formation of the surfactant and velocity profiles as follows. The diffusion term in the Γ equation is relatively small compared with the advection term, so that in the steady state the advection term balances with the adsorption–desorption flux. Integrating the Γ equation with the zero flux condition at the nose of the bubble yield $\Gamma u_\theta = 0$. The front side is surfactant free ($\Gamma = 0$), resulting in the shear-free condition. Therefore, the interface can be mobile and the velocity profile close to that of the clean interface. On the other hand, u_θ must be zero in the rear side because of the non-zero values of Γ. The size of the clean interface region decreases with increasing the Marangoni effect (Ma). As shown in Fig. 12(g), the interfacial vorticity ω_ϕ exhibits a significant peak, the angle of which may correspond to the stagnant-cap angle. At large θ, the contaminated bubbles show negative values of ω_ϕ because of a flow separation like the solid sphere. Since the peak values of ω_ϕ are larger than ω^S_{max}, it is obvious that C_D of the contaminated bubbles cannot be correlated neither with $16\omega_{max}/Re$ nor with $(11\omega_{max} + 7.5)/Re$. The solid lines in Fig. 12(d), (e) and (f) represent the interfacial surfactant concentration Γ, which takes values larger than Γ_{eq} in the rear part of the bubble although u_θ is small. The bulk concentration, C_S, at interface is larger than the bulk concentration when $\Gamma > \Gamma_{eq}$ (Cuenot et al., 1997; Hayashi et al., 2022). The peak of ω_ϕ appears around the angle for $\Gamma = \Gamma_{eq}$.

Fig. 12(b) shows u_θ at $La = 1$. The increase in La (contamination level) largely decreases u_θ. The interfaces at $Ma = 20$ and 40 are almost immobile, which can also be confirmed in Fig. 12(h), i.e., ω_ϕ in these conditions agree well with that of the solid sphere for $\theta \geq \pi/4$. The Γ profiles have the intersection at $\theta \sim 0.38\pi$, at which $\Gamma \approx \Gamma_{eq}$. Further increase in La up to 10 makes the bubble interface immobile at all the three values of Ma as shown in Fig. 12(c), i.e., u_θ is negligibly small. The Γ at the intersection of the Γ profiles shown in Fig. 12(f) is close to Γ_{eq} as well as in Fig. 12(e). The ω_ϕ agrees with that of the solid sphere; the fully-contaminated spherical bubbles behave like the solid sphere. A brief discussion on the effects of Ha on the Γ profile is given in Appendix E.

Fig. 12(j)–(l) show the adsorption–desorption flux $\dot{S}_\Gamma$. As clearly observed in Fig. 12(j), the profile is quite different from that for $Re = Pe = Pe_S = 1$, i.e., $\dot{S}_\Gamma$ is almost constant in the front part of small θ while it begins to decrease at certain θ, at which ω_ϕ steeply increases. The desorption becomes dominant in the rear part of the bubble, so that surfactant molecules are shed from the interface to the bulk and C_S takes values larger than unity (the bulk concentration) as shown in Fig. 12(m). The magnitude of $\dot{S}_\Gamma$ decreases with increasing La and Ma, in particular $\dot{S}_\Gamma$ is close to zero in Fig. 12(l), for which the advection and diffusion terms are both small because of $u_\theta \approx 0$ and $Pe = 100$, and therefore, $\dot{S}_\Gamma$ must be small to balance with those terms.

Fig. 13 reports the non-dimensional group $C_D Re$ as a function of the maximum surface vorticity ω_{max} for $Re = Pe = Pe_S = 100$. The data widely scatter, and no unique relationship between ω_{max} and $C_D Re$ is observed. The data are classified in terms of $\Pi_H = Ha/La$ values. ω_{max} for low Π_H tends to lie on the right-hand side of Eq. (24) for solid spheres because of the formation of the sharp peaks in ω_ϕ. On the other hand, at large Π_H, most of the data are in-between the clean bubble (Eq. (18)) and solid particle equations (Eq. (24)). Fig. 14(a) shows the normalized drag coefficient ξ plotted against ω_{max}. The data of

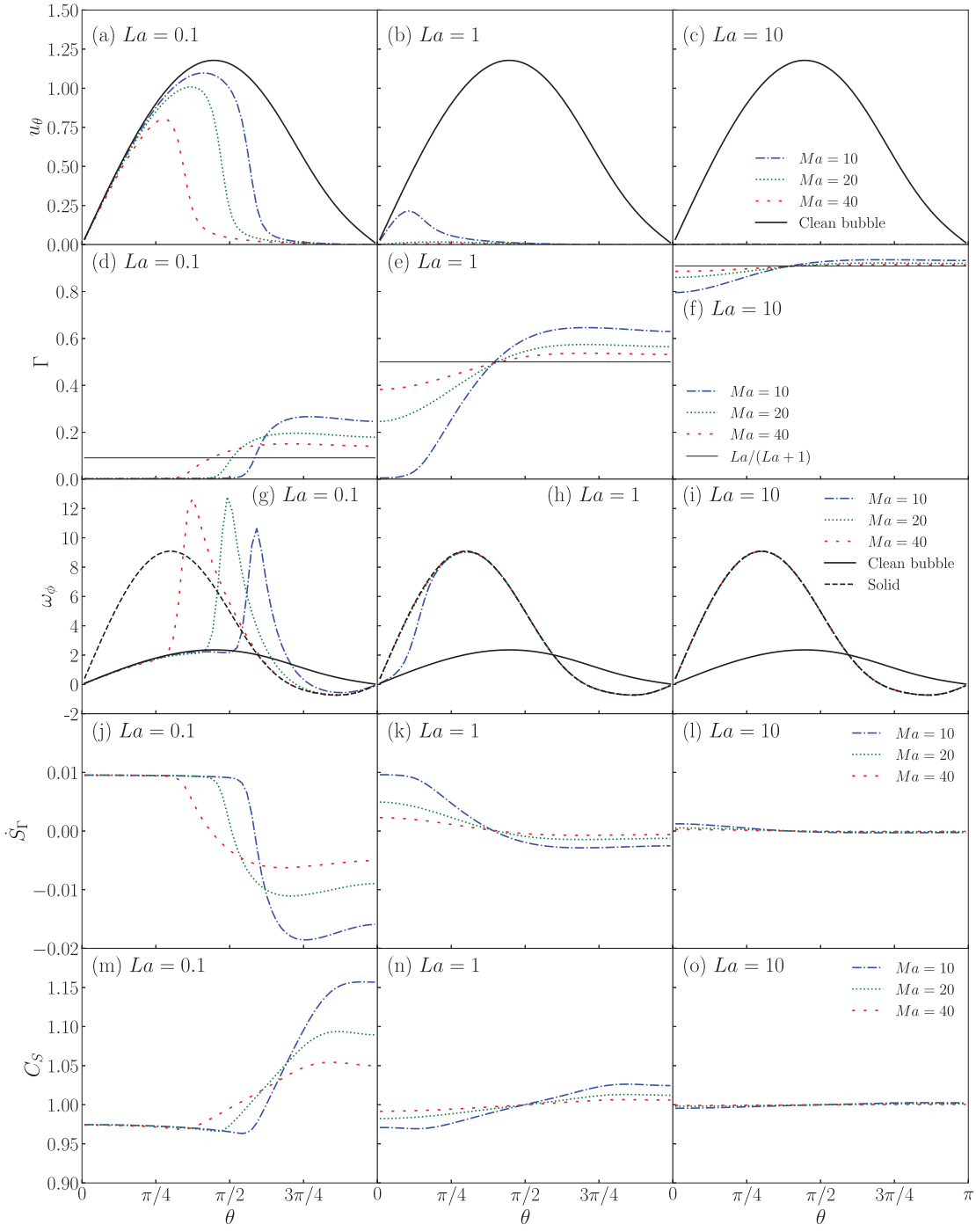

Fig. 12. Profiles of tangential velocity u_θ, surfactant concentration Γ, interfacial vorticity ω_ϕ, adsorption–desorption flux $\dot{S}_\Gamma$ and bulk concentration at interface C_S at $Ha = 0.01$ ($Re = Pe = Pe_S = 100$).

large Π_H distribute within the range of $[\omega^B_{max}, \omega^S_{max}]$. The dashed lines, $\xi = [(\omega_{max} - \omega^B_{max})/16.4]^{0.57}$ and $\xi = [(\omega_{max} - \omega^B_{max})/6.6]^{0.57}$, are fitting curves for the left-most data points. These curves show the dependence on ξ with the same power, 0.57. In Fig. 14(b) the ξ data are plotted against the normalized vorticity

$$\zeta = \frac{\bar{\omega} - \bar{\omega}^B}{\bar{\omega}^S - \bar{\omega}^B} \tag{49}$$

where $\bar{\omega}$ is the mean vorticity defined by $\bar{\omega} = \int_S \omega_\phi dS / \int_S dS$ and is an indicator of the amount of the vorticity increased by the surfactant effect. It should be noted that assuming the fore-aft symmetry in the vorticity profile of a clean bubble, i.e., $\omega_\phi = \omega^B_{max} \sin\theta$, yields $\bar{\omega}^B = \pi\omega^B_{max}/4 \propto \omega^B_{max}$. The $\bar{\omega}$ does not exceed unity and the scatter of the data is mitigated compared with the plots with ω_{max}; especially the data for $\xi < 0.25$ collapse onto the single curve expressed by $\xi = 1.36\zeta^{1.21}$. The increase in the drag due to the surfactant effect exhibits a slightly higher exponent, 1.21, than that in the drag-vorticity relation, Eq. (18), for a clean bubble. In the latter, the drag increase is related with the increase in ω_{max} while keeping the shear-free condition and the fore-aft symmetry in the vorticity profile, while in the former the

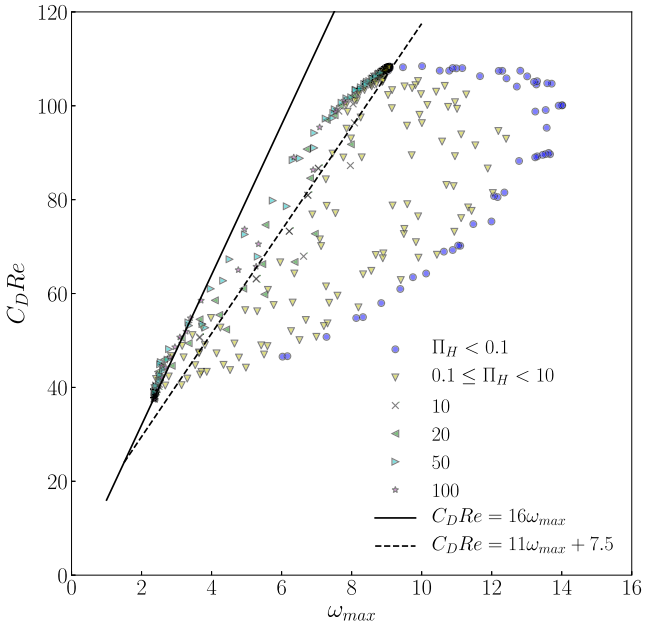

Fig. 13. $C_D Re$ plotted against maximum interfacial vorticity ($Re = Pe = Pe_S = 100$).

Marangoni stress causes a finite tangential viscous stress at the interface and the symmetry breaks down. This may be the cause of the different exponents.

Fig. 15 shows ξ for several values of Π_H. ξ is proportional to Π_M at small ξ as shown by the dashed lines, that is $\xi = \alpha\Pi_M$. The coefficient, α, decreases with increasing Π_H due to the smoothing effect of Π_H. On the other hand, comparison of the data of $\Pi_H = 50$ with $La = 0.02$ (the closed symbols) and 0.12 (the open symbols) clearly demonstrates that La increases ξ. It should however be noted that α becomes independent of La in the limiting case of $\Pi_H \to 0$, being similar to the diffusion-dominant case. The regime in which ξ is proportional to Π_M corresponds to the range in which $\xi = 1.36\zeta^{1.21}$ shown in Fig. 14(b). The data start to deviate from the linear fits as Π_M increases, i.e., the increasing rate mitigates. The nonlinear dependence is clearer in Fig. 16, where the C_D data at the intermediate Π_M range lie on the curve represented by $C_D = b\Pi_M^{0.362}$, where b depends on Π_H and La. Equivalently, $\xi = \gamma\Pi_M^{0.362} - c$, where $\gamma = b/(C_D^S - C_D^B)$ and $c = C_D^B/(C_D^S - C_D^B)$.

The dependence of ξ on Π_M at large Π_M is shown in Fig. 17. For $\Pi_H = 0.5$ and 1, the decay of $1 - \xi$ for Π_M smaller than about 10 is not linear but can be expressed as $1 - \xi = \delta/\Pi_M^{2.5}$ by tuning the value of δ (the dashed lines). The ξ is then inversely proportional to Π_M at larger Π_M, i.e., $1 - \xi = \beta/\Pi_M$, as shown by the solid lines. In these two conditions La is the same, and therefore, the difference in the data is attributed to the Π_H effect. For the larger Π_H (20 and 50), the dependence on Π_M with the power of 2.5 does not appear. The data of $\Pi_H = 50$ lie below those of $\Pi_H = 20$, showing that the increase in La enhances the contamination and its effect is remarkable at large Π_H.

Summarizing the results obtained above for the advection-dominant case gives the following expression for ξ where the regime I and IV identified for the diffusion-dominant case are also observed:

$$\xi = \frac{C_D - C_D^B}{C_D^S - C_D^B} = \begin{cases} \alpha\Pi_M & \text{(Regime I)} \\ \gamma\Pi_M^{0.36} - c & \text{(Regime II)} \\ 1 - \delta/\Pi_M^{2.5} & \text{(Regime III)} \\ 1 - \beta/\Pi_M & \text{(Regime IV)} \end{cases} \tag{50}$$

where α, β, γ and δ are functions of Π_H and La, while the effects of these dimensionless groups disappear as $\Pi_H \to 0$ and they become constant. Thus, the regimes are characterized by the dependence of ξ on Π_M as in the diffusion-dominant case, and the functional forms in Regimes I and IV are the same as those in the diffusion-dominant case. Fig. 18 shows a schematic representation of the regimes. The top curve represents ξ for the limiting case of $\Pi_H \to 0$. The ξ increases with increasing Π_M and the regime changes from I to IV along the curve. Regime III appears only in the upper-left region of small Π_H. The increase in Π_H changes the curve toward the mobile-interface side. The La has the opposite effect, which however vanishes in the low Π_H limit. Note that the stagnant-cap (IS-c) surface state is also observed for Regime I at small $\Pi_H = Ha/La$. This is another reason that justifies the definition of regimes by considering the dependence of C_D (or ω) rather than by considering the velocity profile shape.

By writing the vorticity given in Eq. (22) as ω^S, i.e. $\omega^S = 3(1 + \Phi(Re))/2$, the expression of ξ in Regimes I and IV can be written as

$$\frac{C_D Re}{16} = \begin{cases} \omega_{max}^B + \left(\omega^S - \omega_{max}^B\right)\alpha\Pi_M & \text{(Regime I)} \\ \omega^S - \frac{\omega^S - \omega_{max}^B}{\Pi_M/\beta} & \text{(Regime IV)} \end{cases} \tag{51}$$

These functional forms are similar to those of Eqs. (36) and (39), respectively, for ω_{max}, and in these limiting cases the R.H.S. can be employed as ω for the expression of $C_D Re = 16\omega$ at $Re = Pe = 100$. ξ exhibits the nonlinear behavior at intermediate Π_M corresponding to Regimes II and III, which makes the dependence of ξ on the relevant dimensionless groups more complicated compared with those in Regimes I and IV.

4.5. Stagnant-cap angle

For some situations of the advection dominant case ($Re = Pe = Pe_S = 100$), ω_ϕ possesses a peak in its profile as shown in Fig. 3(a). These cases are therefore representative of the stagnant-cap interface (IS-c) state. The normalized drag coefficient ξ has a unique relation with Π_M when $\Pi_H \ll 1$ (Fig. 15) and can be expressed as a function of the angle θ_{cap} as demonstrated in Fig. 19(a), where θ_{cap} is defined as the angle for ω_{max} (the peak in the ω_ϕ profile) and the data are for $\Pi_H \le 0.1$. Cuenot et al. (1997) also pointed out that ξ is correlated well with θ_{cap} only. Their numerical data of ξ are in good agreement with the present ones as shown in the figure. This fact supports that the reduction in Pe from 10^5 to 100 does not have a significant impact on the drag as reported by Takagi et al. (2003) and Fukuta et al. (2008). Although the Sadhal–Johnson model (Sadhal and Johnson, 1983) was derived for the Stokes flow regime, ξ fairly agreed with the numerical results of Cuenot et al. (1997) for $Re = 100$. For the stagnant-cap model, ξ is given by (Dani et al., 2022)

$$\xi(\theta_{cap}) = 1 - \frac{\theta_{cap}}{\pi} + \frac{1}{2\pi}\left(\sin\theta_{cap} + \sin 2\theta_{cap} - \frac{\sin 3\theta_{cap}}{3}\right) \tag{52}$$

where $\theta_{cap} = 0$ represents fully-immobile interface ($\xi(0) = 1$) and $\theta_{cap} = \pi$ is for clean interface ($\xi(\pi) = 0$). The ξ data are compared with the Sadhal–Johnson model in Fig. 19(b) (the dashed line). A reasonable agreement is obtained for Regimes II and III. This result suggests that the angle for ω_{max} for the stagnant-cap bubbles can be taken as θ_{cap} in evaluation of ξ. The dash-dotted line in the figure demonstrates that Eq. (52) can be adjusted for the numerical data by replacing the two factors in the third term as $1/2\pi \to 0.228$ and $\sin\theta_{cap} \to 0.62\sin\theta_{cap}$. The following simple fitting equation can also represent the numerical results well as shown by the solid line:

$$\xi(\theta_{cap}) = \frac{1}{2\exp\left(0.010\,\theta_{cap}^{6.19}\right) - 1} \tag{53}$$

Fig. 19(b) shows θ_{cap} as a function of Π_M. The θ_{cap} is correlated well in terms of Π_M only as given by the following correlation:

$$\theta_{cap} = \pi(1 - 0.407\,\Pi_M^{0.314}) \tag{54}$$

This empirical correlation would be of great interest for estimating the cap angle. This is the first time to propose a model of θ_{cap} in terms of the relevant dimensionless groups controlling the contamination effects.

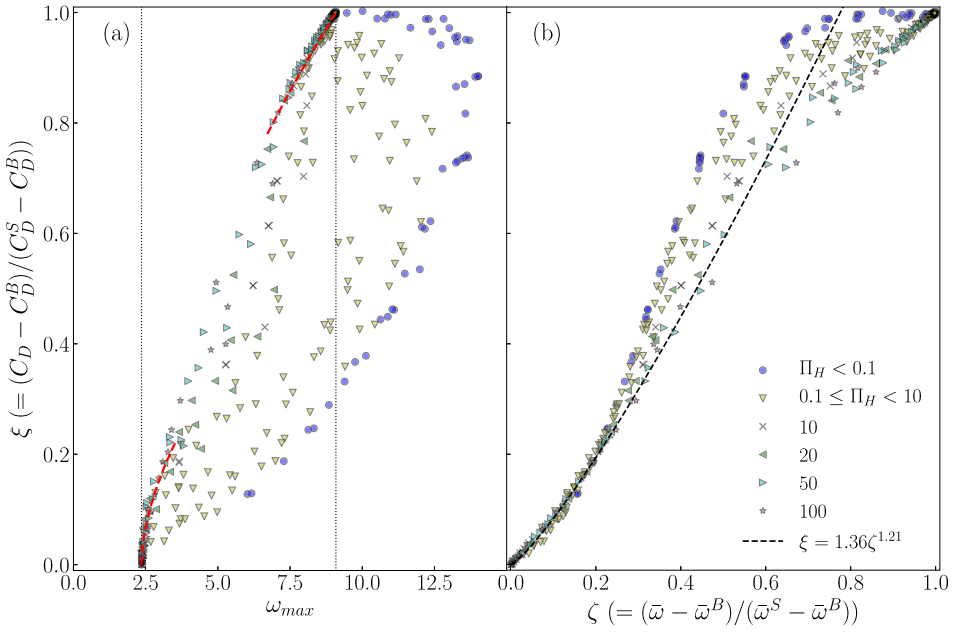

Fig. 14. Normalized drag coefficient, ξ, plotted against interfacial vorticity ($Re = Pe = Pe_S = 100$). The left and right dotted lines in (a) represent ω_{max} of clean bubble and solid particle, respectively. The dashed lines in (a) are $\xi = [(\omega_{max} - \omega^B_{max})/16.4]^{0.57}$ and $\xi = [(\omega_{max} - \omega^B_{max})/(\omega^S_{max} - \omega^B_{max})]^{0.57}$.

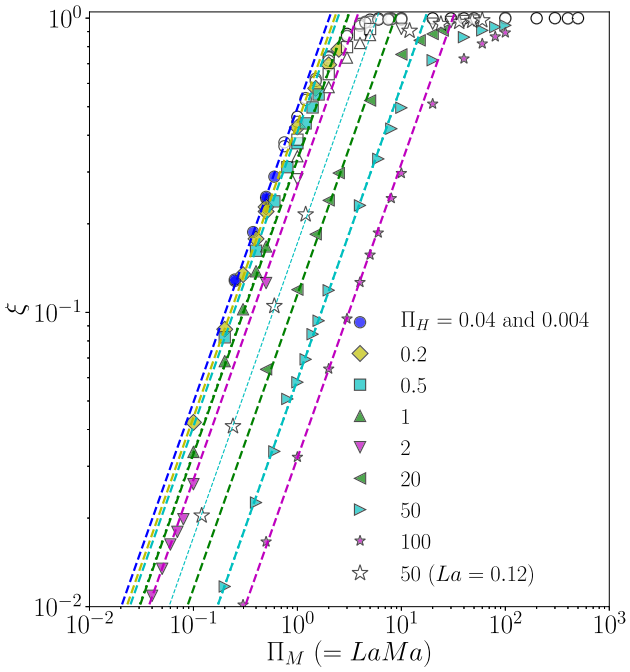

Fig. 15. Normalized drag coefficient ξ and linear regressions for small Π_M range ($Re = Pe = Pe_S = 100$). The closed symbols are for $La \le 0.05$, while the open symbols are for $La = 0.1$ ($\Pi_H \ne 50$), 0.12 ($\Pi_H = 50$) or $La > 0.05$ ($\Pi_H < 0.1$). The dashed lines are linear fit, $\xi \propto \Pi_M$, to the data. The slopes, α, of the lines for $La \le 0.05$ are $\alpha = 0.50$, 0.44, 0.41, 0.33, 0.27, 0.115, 0.059 and 0.032 for $\Pi_H < 0.1$, $\Pi_H = 0.2$, 0.5, 1, 2, 20, 50, and 100, respectively, and $\alpha = 0.17$ for $(\Pi_H, La) = (50, 0.12)$.

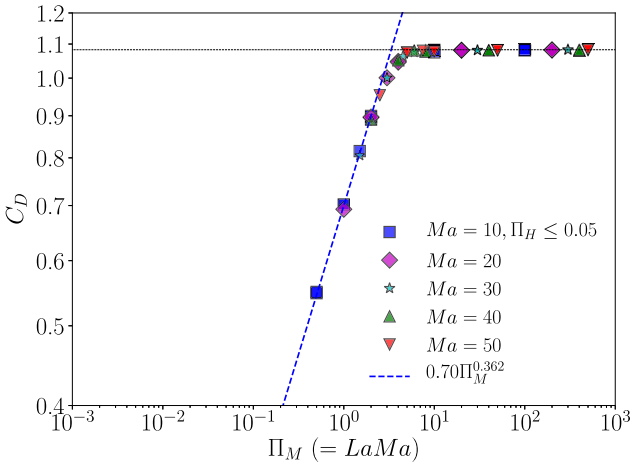

Fig. 16. Drag coefficient plotted against Π_M. The data are for $\Pi_H \le 0.05$ ($Re = Pe = Pe_S = 100$).

5. Conclusion

In the present study, effects on soluble surfactant on the interfacial vorticity and the drag coefficient of a spherical bubble were numerically investigated. This study is the first to propose their expressions in terms of the relevant dimensionless groups and to investigate the drag-vorticity relations in detail. As a result, the following conclusions were obtained:

1. $C_D Re = 16\omega_{max}$ originally proposed for clean bubbles is valid also for contaminated bubbles in the diffusion-dominant case, i.e., $Re = Pe = Pe_S = 1$.
2. The key dimensionless group for the degree of contamination in expressing ω_{max} is $\Pi_M = LaMa$ as suggested by the boundary condition and the adsorption–desorption kinetics.
3. Increase in the Hatta number makes the surfactant concentration profile smoother, mitigating the Marangoni effect, and $\Pi_H = Ha/La$ also plays an important role in determining the interfacial vorticity.
4. The characteristics of C_D and ω_{max} in the advection-dominant case ($Re = Pe = Pe_S = 100$) are more complicated and there is no unique relation between them, but they can be classified into four regimes in terms of $\Pi_M = LaMa$ and $\Pi_H = Ha/La$.

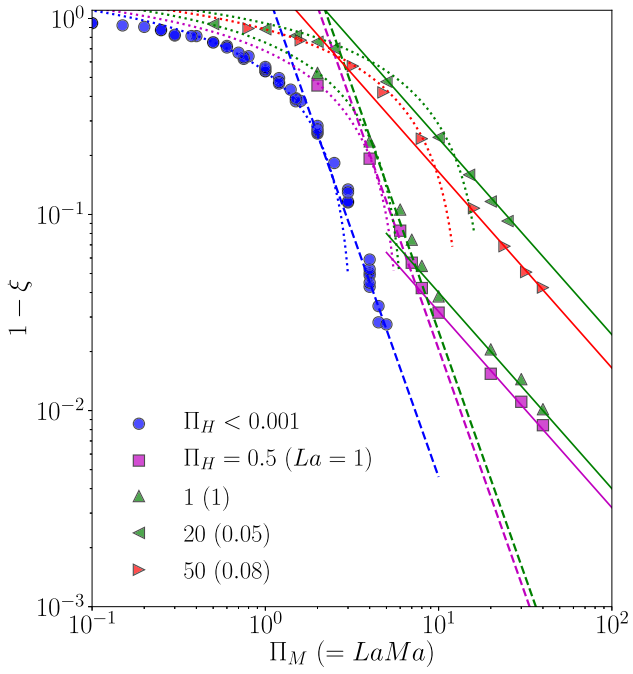

Fig. 17. Characteristics of normalized drag coefficient ξ ($Re = Pe = Pe_S = 100$). The values in the legend represent Π_H. The coefficients, δ, in $\xi = 1-\delta/\Pi_M^{2.5}$ are 1.5, 6.5, 8.0 for $\Pi_H < 0.001$, $(\Pi_H, La) = (0.5, 1)$, and $(1, 1)$, respectively, and those in $1-\xi = \beta/\Pi_M$ are 0.32, 0.40, 2.44, and 1.65 for $(\Pi_H, La) = (0.5, 1)$, $(1, 1)$, $(20, 0.05)$, and $(50, 0.08)$, respectively.

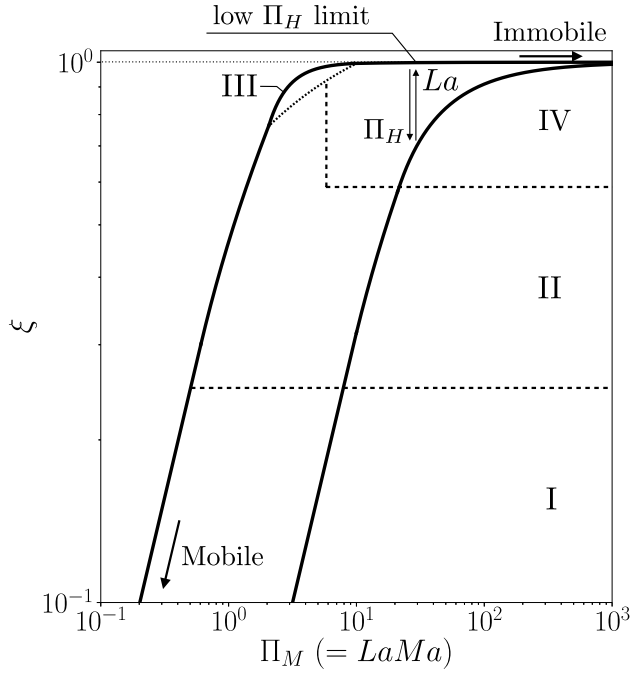

Fig. 18. Schematic representation of the four regimes observed for the advection-dominant case ($Re = Pe = Pe_S = 100$). The dashed lines represent the regime boundaries. The upper solid line represents the ξ curve in the low Π_H limit. The Π_H effect moves the curve and the curve connects the mobile (IS-a) interface to the immobile (IS-d) interface.

5. A simple expression of the stagnant-cap angle θ_{cap} in terms of $\Pi_M = LaMa$ was obtained for the stagnant-cap (IS-c) state appearing at small $\Pi_H = Ha/La$

Table 1
Summary of drag and vorticity correlations.

Diffusion-dominant case
$C_D = 16\omega_{max}/Re$ (Regimes I, IV and in-between)
$\omega_{max} = \frac{\omega^B_{max}+\omega^S_{max}c_w\Pi_M/(1+\Psi)}{1+c_w\Pi_M/(1+\Psi)}$ with $\Psi = (0.03La + 0.115)\Pi_H$ and $c_w = 1/7.0$
$\xi = \frac{C_D-C_D^B}{C_D^S-C_D^B} = \left\{1+\frac{1+\Psi}{c_w\Pi_M}\right\}^{-1}$
Advection-dominant case[a]
$C_D = \begin{cases}\frac{16}{Re}\left(\omega^B_{max}+\left(\omega^S-\omega^B_{max}\right)\alpha\Pi_M\right) & \text{(Regime I)}\\ \frac{16}{Re}\left(\omega^S-\frac{\omega^S-\omega^B_{max}}{\Pi_M/\beta}\right) & \text{(Regime IV)}\end{cases}$ with $\omega^S = \frac{3}{2}\left(1+0.15Re^{0.687}\right)$
$\xi = \begin{cases}\alpha\Pi_M & \text{(Regime I)}\\ \gamma\Pi_M^{0.36}-c & \text{(Regime II)}\\ 1-\delta/\Pi_M^{2.5} & \text{(Regime III)}\\ 1-\beta/\Pi_M & \text{(Regime IV)}\end{cases}$
$\xi(\theta_{cap}) = \left\{2\exp\left(0.010\,\theta_{cap}^{6.19}\right)-1\right\}^{-1}$ with $\theta_{cap} = \pi(1-0.407\,\Pi_M^{0.314})$ (for stagnant-cap states)

[a] The coefficients α (Fig. 15), β (Fig. 17), δ (Fig. 17), γ (Fig. 16) depend on Π_H and La, and values found in the present study are as follows: α for $La \le 0.05$ are 0.50, 0.44, 0.41, 0.33, 0.27, 0.115, 0.059 and 0.032 for $\Pi_H < 0.1$, $\Pi_H = 0.2$, 0.5, 1, 2, 20, 50, and 100, respectively, and $\alpha = 0.17$ for $(\Pi_H, La) = (50, 0.12)$; $\beta = 0.32$, 0.40, 2.44, and 1.65 for $(\Pi_H, La) = (0.5, 1)$, $(1, 1)$, $(20, 0.05)$, and $(50, 0.08)$; $\delta = 1.5$, 6.5, 8.0 for $\Pi_H < 0.001$, $(\Pi_H, La) = (0.5, 1)$, and $(1, 1)$; $\gamma = 0.70/(C_D^S - C_D^B)$ for $\Pi_H \ll 1$.

Table 1 summarizes the drag and vorticity correlations obtained in the present study.

This work is limited to bubbles of spherical shape, so that the influence of the shape deformation on the Marangoni effect should be further investigated in the future. Deformation of a bubble increases the magnitude of the interfacial vorticity since the interface curvature (the first term of Eq. (28)) is increased at the bubble equator (Atasi et al., 2023). As a consequence, for small deformation, both deformation and contamination effects can be added in the resulting interfacial vorticity distribution.

CRediT authorship contribution statement

Kosuke Hayashi: Writing – original draft, Visualization, Methodology, Investigation, Funding acquisition, Formal analysis, Conceptualization. **Yuya Motoki:** Writing – original draft, Methodology, Investigation, Formal analysis. **Dominique Legendre:** Writing – original draft, Methodology, Investigation, Conceptualization. **Akio Tomiyama:** Writing – original draft, Methodology, Investigation, Conceptualization.

Declaration of competing interest

The authors declare that they have no known competing financial interests or personal relationships that could have appeared to influence the work reported in this paper.

Acknowledgments

This work was supported by JKA and its promotion funds from AUTORACE and by JSPS KAKENHI Grant Number 24K00805.

Appendix A. Ranges of dimensionless groups in typical contaminated systems

Cuenot et al. (1997) used the physical properties of decanoic acid for the reference case, while Triton X-100 and 1-pentanol were used in the experiments and numerical simulations carried out by Takagi et al. (2003). Varying the bulk concentration of decanoic acid from 1 mmol/m^3 to 100 mmol/m^3 yields the following ranges of La, Ma, Ha and K for a 1 mm bubble rising through water at 0.1 m/s: $0.011 \le La \le 1.1$, $Ma = 124$, $4\times10^{-4} \le Ha \le 4\times10^{-2}$ and $0.2 \le K \le 20$. Takagi et al.

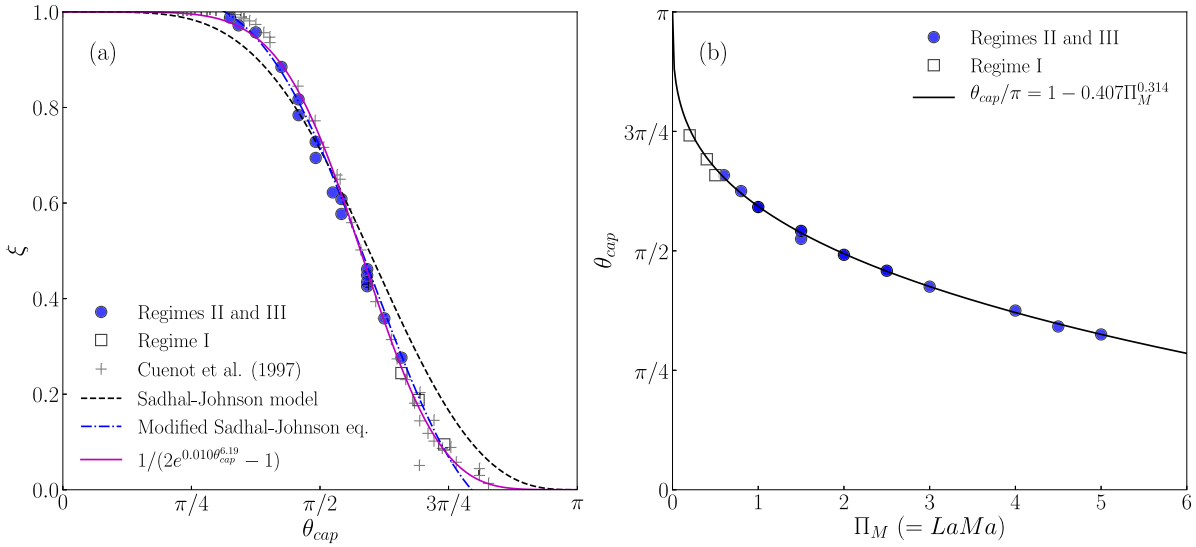

Fig. 19. Relation between stagnant cap angle, θ_{cap}, (the angle for ω_{max}(the peak of ω_ϕ)) and normalized drag coefficient, ξ (a), and θ_{cap} as a function of Π_M (b). The dashed, solid and dash-dotted lines in (a) are Eqs. (52), (53) and $\xi(\theta_{cap}) = \max\left\{0, \min\left[1-\theta_{cap}/\pi + 0.228\left(0.62\sin\theta_{cap} + \sin 2\theta_{cap} - (\sin 3\theta_{cap})/3\right), 1\right]\right\}$, respectively. The solid line in (b) is the fitting equation, $\theta_{cap}/\pi = 1 - 0.407\Pi_M^{0.314}$. Ma ranges from 10 to 50, La ranges from 0.02 to 0.1, and $\Pi_H \le 0.1$ in the plotted data. ($Re = Pe = Pe_S = 100$).

(2003) used Triton X-100 of $C_0 \sim 1$ mmol/m^3 in their experiments. Higher concentrations, e.g., 10 mmol/m^3 (Hori et al., 2020), have also often been used in experiments on bubbles. For the range of $1 \le C_0 \le 10$ mmol/m^3, $1.5 \le La \le 15$, $Ma = 70$, $5\times10^{-4} \le Ha \le 5\times10^{-3}$, and $0.34 \le K \le 3.4$. Compared with Triton X-100, much higher concentrations have been used for 1-pentanol, i.e., 40–690 mmol/m^3 in Takagi et al. (2003) and 12,000 mmol/m^3 in Aoki et al. (2017). For the range of $10 \le C_0 \le 10{,}000$ mmol/m^3, $0.00046 \le La \le 0.46$, $Ma = 146$, $5\times10^{-4} \le Ha \le 0.5$, and $1.7 \le K \le 1700$. The Langmuir number for 1-pentanol is smaller than that for Triton X-100 although the bulk concentration is much larger in the former. This is because of the large desorption rate coefficient.

The bubble of $Re = 1$ corresponds to that of $d = 0.13$ mm and $U = 7.8$ mm/s in contaminated water. For the same range of C_0 as in the above discussion for $Re = 100$, the ranges of Ma, Ha and K are as follows. For decanoic acid: $Ma = 1600$, $6\times10^{-4} \le Ha \le 6\times10^{-2}$ and $0.026 \le K \le 2.6$; for Triton X-100: $Ma = 920$, $8\times10^{-4} \le Ha \le 8\times10^{-3}$ and $0.044 \le K \le 0.44$; for 1-pentanol: $Ma = 1880$, $8\times10^{-4} \le Ha \le 0.8$ and $0.22 \le K \le 220$. The Ma in the actual system can be very large. This is one of the reasons why the rise motion of a small bubble is easily retarded by only a small amount of surfactant. The condition of $Re = Pe = 1$ is similar to that for the drop motion analyzed by Frumkin and Levich (1947); the main assumptions in their analysis are the Stokes motion of the fluids, the sinusoidal profile of the interfacial velocity, and a slight deviation from the surfactant concentration at the adsorption–desorption equilibrium. Therefore, the case of $Re = Pe = 1$ may be regarded as an extension of the case dealt with by Frumkin and Levich (1947).

Appendix B. Effects of dimensionless adsorption length, K

The dimensionless adsorption length, K, was set to unity in all the simulations discussed above. The K might affect the result through the boundary condition of the bulk concentration, C, Eq. (13). The meaning of K can be understood as follows: for the interface of a spherical bubble fully packed by surfactant, the surfactant mole adsorbed on the interface is $n_S = \Gamma_{max} 4\pi a^2$. By assuming that this amount of surfactant came from the shell region surrounding the bubble, the surfactant mole in this region is $n_V = C_0(4\pi/3)[(a+\Delta)^3 - a^3]$, where Δ is the width of the shell. Equating n_S and n_V yields

$$K = \frac{\Delta}{d}\left[1 + 2\frac{\Delta}{d} + \frac{4}{3}\left(\frac{\Delta}{d}\right)^2\right] \tag{B.1}$$

In a sense of the order of magnitude, C varies in $[a, a+\Delta]$; K is thus one of the factors scaling $\partial C/\partial r|_{r=a}$.

Numerical simulations were carried out at $K = 0.1$ and 10 to understand the effects of K on ω_ϕ. Fig. B.20(a) and (b) show ω_ϕ at $Re = Pe = 1$ and $Re = Pe = 100$, respectively, and the other parameters are $Ma = 10$, $La = 0.1$ and $Ha = 0.01$. No differences are observed in the vorticity profiles at these values of K. Therefore, K does not substantially affect ω_ϕ, i.e. the bubble dynamics, in the range of K tested.

Appendix C. Drag-vorticity relation for solid spheres

Although Eq. (24) reproduces the trend of $C_D Re$ for a wide range of Re, Eq. (22) gives a better estimation for small Re, i.e. $Re \le 10$, at which no flow separation takes place at the solid surface. Tuning the coefficients in Eq. (24) for $Re \ge 1$ and switching the expressions depending on Re yield

$$C_D Re = \min\left[16\omega_{max}^S, 10.88\,\omega_{max} + 8.8\right] \tag{C.1}$$

Appendix D. Effect of Péclet number on vorticity profile

Fig. D.21 compares the interfacial vorticity with $Pe = 100$ (shown in Fig. 12) and that with $Pe = 10^5$. Note that $Pe_S = 100$ in both cases. For $La = 0.10$, the vorticity distribution is not affected so much even with the significant change in Pe, that is, in both cases the stagnant-cap states are formed. With the larger La ($La = 1$), the difference between the vorticity distributions with $Pe = 100$ and 10^5 is smaller. Thus, Pe is not of primal importance when it is already much larger than unity. This fact supports that numerical simulations with spatial resolutions insufficient to resolve thin boundary layers could give reasonable results in literature.

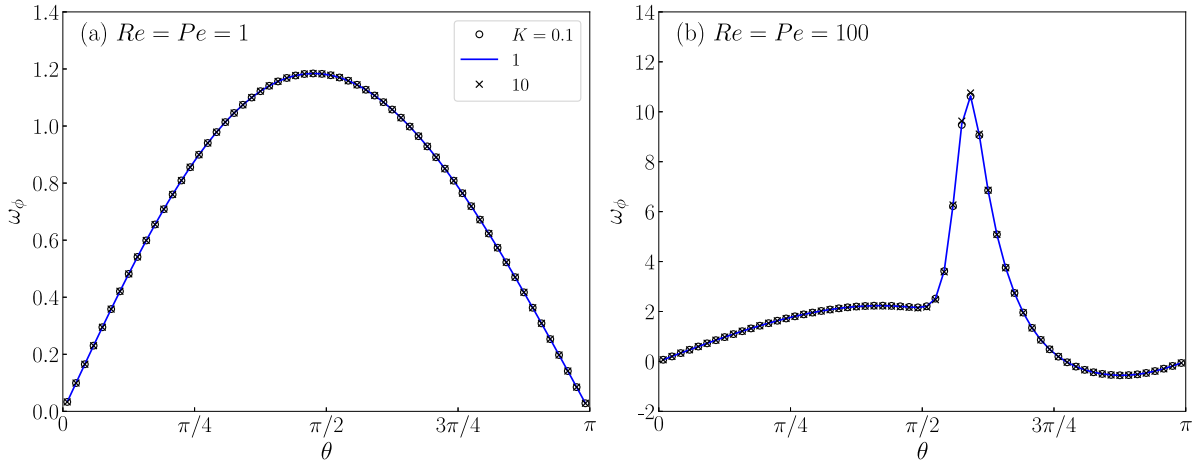

Fig. B.20. Comparisons between ω_ϕ at $K = 0.1$, 1 and 10.

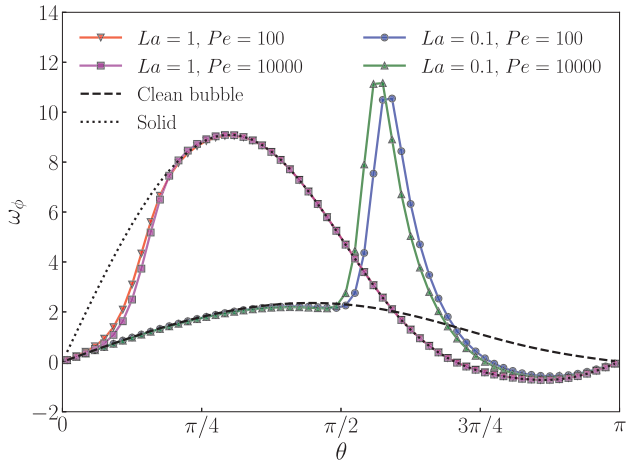

Fig. D.21. Interfacial vorticity predicted with $Pe = 100$ and 10000 ($Ma = 10$ and $Ha = 0.01$).

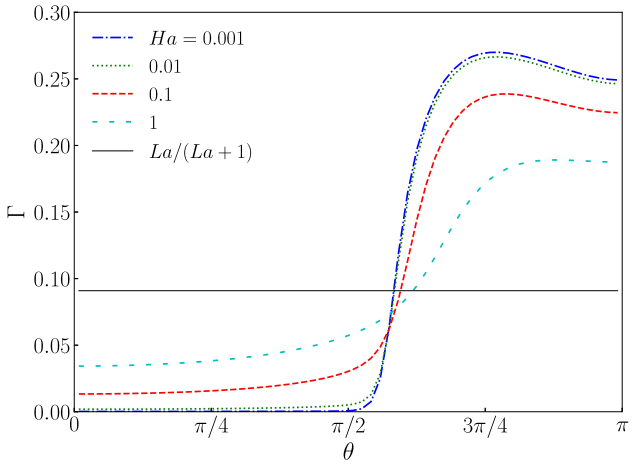

Fig. E.22. Profiles of Γ at $La = 0.1$ and $Ma = 10$.

Appendix E. Effects of Ha on Γ profile

The effect of Ha on Γ at $Re = Pe = 100$ is shown in Fig. E.22. The increase in Ha makes the Γ profile smoother, which, in turn, means Ha mitigates the Marangoni effect. It should however be noted that the Ha effect on the Γ profile is not remarkable at the small values of Ha. The mean concentrations, $\int_S \Gamma dS / \int_S dS$, are also not so much affected by Ha, i.e., 0.091, 0.091, 0.089 and 0.084 at $Ha = 0.001$, 0.01, 0.1 and 1, respectively, and are similar to Γ_{eq} (= 0.909).

Data availability

Data will be made available on request.

References

Adoua, R., Legendre, D., Magnaudet, J., 2009. Reversal of the lift force on an oblate bubble in a weakly viscous linear shear flow. J. Fluid Mech. 628, 23–41.

Aoki, J., Hori, Y., Hayashi, K., Hosokawa, S., Tomiyama, A., 2017. Mass transfer from single carbon dioxide bubbles in alcohol aqueous solutions in vertical pipes. Int. J. Heat Mass Transfer 108, 1991–2001.

Aoyama, S., Hayashi, K., Hosokawa, S., Tomiyama, A., 2016. Shapes of ellipsoidal bubbles in infinite stagnant liquids. Int. J. Multiph. Flow 79, 23–30.

Atasi, O., Haut, B., Pedrono, A., Scheid, B., Legendre, D., 2018. Influence of soluble surfactants and deformation on the dynamics of centered bubbles in cylindrical microchannels. Langmuir 34, 10048–10062.

Atasi, O., Ravisankar, M., Legendre, D., Zenit, R., 2023. Presence of surfactants controls the stability of bubble chains in carbonated drinks. Phys. Rev. Fluids 8, 053601.

Batchvarov, A., Kahouadji, L., Magnini, M., Constante-Amores, C.R., Shin, S., Chergui, J., Juric, D., Craster, R.V., Matar, O.K., 2020. Effect of surfactant on elongated bubbles in capillary tubes at high Reynolds number. Phys. Rev. Fluids 5 (9), 093605.

Blanco, A., Magnaudet, J., 1995. The structure of the axisymmetric high-Reynolds number flow around an ellipsoidal bubble of fixed shape. Phys. Fluids 7 (6), 1265–1274.

Chang, C.-H., Franses, E.I., 1995. Adsorption dynamics of surfactants at the air/water interface: a critical review of mathematical models, data, and mechanisms. Colloids Surf. A Physicochem. Eng. Asp. 100, 1–45.

Chen, J., Hayashi, K., Hosokawa, S., Tomiyama, A., 2019. Drag correlations of ellipsoidal bubbles in clean and fully-contaminated systems. Multiph. Sci. Technol. 31 (3), 215–234.

Choi, H., Moin, P., 1994. Effects of the computational time step on numerical solutions of turbulent flow. J. Comput. Phys. 113 (1), 1–4.

Clift, R., Grace, J., Weber, M., 1978. Bubbles, Drops, and Particles. Academic Press.

Constante-Amores, C.R., Chergui, J., Shin, S., Juric, D., Castrejón-Pita, J.R., Castrejón-Pita, A.A., 2022. Role of surfactant-induced marangoni stresses in retracting liquid sheets. J. Fluid Mech. 949, A32.

Constante-Amores, C.R., Kahouadji, L., Batchvarov, A., Shin, S., Chergui, J., Juric, D., Matar, O.K., 2021. Dynamics of a surfactant-laden bubble bursting through an interface. J. Fluid Mech. 911, A57.

Cuenot, B., Magnaudet, J., Spennato, B., 1997. The effects of slightly soluble surfactants on the flow around a spherical bubble. J. Fluid Mech. 339, 25–53.
Dani, A., Cockx, A., Guiraud, P., 2006. Direct numerical simulation of mass transfer from spherical bubbles: the effect of interface contamination at low Reynolds numbers. Int. J. Chem. React. Eng. 4 (1).
Dani, A., Cockx, A., Legendre, D., Guiraud, P., 2022. Effect of spheroid bubble interface contamination on gas-liquid mass transfer at intermediate Reynolds numbers: From DNS to sherwood numbers. Chem. Eng. Sci. 248 (116979), 116979.
Dukhin, S.S., Kretzschmar, G., Miller, R., 1995. Dynamics of Adsorption at Liquid Interfaces. Elsevier Science, Netherlands.
Frumkin, A., Levich, V.G., 1947. On surfactants and interfacial motion (in Russian). Zh. Fiz. Khim. 21, 1183–1204.
Fukuta, M., Takagi, S., Matsumoto, Y., 2008. Numerical study on the shear-induced lift force acting on a spherical bubble in aqueous surfactant solutions. Phys. Fluids 20 (4), 040704.
Hadamard, J.S., 1911. Mouvement permanent tent d'une sphere liquide et visquese dans un liquide visqueux. C. R. I'Acad. Sci. 152, 1735–1738.
Harper, J.F., 1982. Surface activity and bubble motion. Appl. Sci. Res. 38 (1), 343–352.
Hayashi, K., Hessenkemper, H., Lucas, D., Legendre, D., Tomiyama, A., 2021. Scaling of lift reversal of deformed bubbles in air-water systems. Int. J. Multiph. Flow 142, 103653.
Hayashi, K., Legendre, D., Tomiyama, A., 2020. Lift coefficients of clean ellipsoidal bubbles in linear shear flows. Int. J. Multiph. Flow 129, 103350.
Hayashi, K., Motoki, Y., van der Linden, M.J.A., Deen, N.G., Hosokawa, S., Tomiyama, A., 2022. Single contaminated drops falling through stagnant liquid at low Reynolds numbers. Fluids 7 (2), 55.
Hayashi, K., Tomiyama, A., 2012. Effects of surfactant on terminal velocity of a Taylor bubble in a vertical pipe. Int. J. Multiph. Flow 39, 78–87.
Hidman, N., Ström, H., Sasic, S., Sardina, G., 2022. The lift force on deformable and freely moving bubbles in linear shear flows. J. Fluid Mech. 952, A34.
Hori, Y., Bothe, D., Hayashi, K., Hosokawa, S., Tomiyama, A., 2020. Mass transfer from single carbon-dioxide bubbles in surfactant-electrolyte mixed aqueous solutions in vertical pipes. Int. J. Multiph. Flow 124, 103207.
Hosokawa, S., Masukura, Y., Hayashi, K., Tomiyama, A., 2017. Experimental evaluation of marangoni stress and surfactant concentration at interface of contaminated single spherical drop using spatiotemporal filter velocimetry. Int. J. Multiph. Flow 97, 157–167.
James, A., Lowengrub, J., 2004. A surfactant-conserving volume-of-fluid method for interfacial flows with insoluble surfactant. J. Comput. Phys. 201, 685–722.
Kentheswaran, K., Antier, W., Dietrich, N., Lalanne, B., 2023. Impact of surfactants on the rise of deformable bubbles and interfacial gas–liquid mass transfer. J. Fluid Mech. 970, A5.
Kentheswaran, K., Dietrich, N., Tanguy, S., Lalanne, B., 2022. Direct numerical simulation of gas-liquid mass transfer around a spherical contaminated bubble in the stagnant-cap regime. Int. J. Heat Mass Transfer 198, 123325.
Kurimoto, R., Hayashi, K., Tomiyama, A., 2013. Terminal velocities of clean and fully-contaminated drops in vertical pipes. Int. J. Multiph. Flow 49, 8–23.
Legendre, D., 2007. On the relation between the drag and the vorticity produced on a clean bubble. Phys. Fluids 19, 018102.
Legendre, D., Sarrot, V., Guiraud, P., 2009. On the particle inertia-free collision with a partially contaminated spherical bubble. Int. J. Multiph. Flow 35 (2), 163–170.
Lerner, L., Harper, J.F., 1991. Stokes flow past a pair of stagnant-cap bubbles. J. Fluid Mech. 232, 167–190.
Levich, V., 1962. Physicochemical Hydrodynamics. Prentice Hall.
Magnaudet, J., Mougin, G., 2007. Wake instability of a fixed spheroidal bubble. J. Fluid Mech. 572, 311–337.
Maxworthy, T., Gnann, C., Kürten, M., Durst, F., 1996. Experiments on the rise of air bubbles in clean viscous liquids. J. Fluid Mech. 321, 421–441.
Mclaughlin, J.B., 1996. Numerical simulation of bubble motion in water. J. Colloid Interface Sci. 184 (2), 614–625.
Mei, R., Klausner, J., Lawrence, C., 1994. A note on the history force on a spherical bubble at finite Reynolds number. Phys. Fluids 6, 418–420.
Ramírez-Muñoz, J., Galicia-Nequiz, O.G., Baz-Rodríguez, S., Colín-Luna, J.A., Martínez-Delgadillo, S.A., Puebla, H., 2012. The effects of surfactants on the drag of a bubble. Procedia Eng. 42, 1840–1848.
Rybczynski, W., 1911. On the translatory of a fluid sphere in a viscous medium. Bull. Acad. Sci. Kracow, Ser. A 40–46.
Sadhal, S.S., Johnson, R.E., 1983. Stokes flow past bubbles and drops partially coated with thin films. Part 1. Stagnant cap of surfactant film – exact solution. J. Fluid Mech. 126 (1), 237–250.
Saffman, P., 1992. Vortex Dynamics. Cambridge University Press.
Savic, P., 1953. Circulation and Distortion of Liquid Drops Falling Through a Viscous Medium. Technical Report MT-22, National Research Council of Canada (NRCC).
Schiller, V.L., Naumann, A.Z., 1933. Uber die grundlegenden berechnungen bei der schwerkraftaufbereitung. Z. Vereines Dtsch. Ingen. 77, 318–320.
Shu, C.-W., Osher, S., 1989. Efficient implementation of essentially non-oscillatory shock-capturing schemes, II. J. Comput. Phys. 83 (1), 32–78.
Stone, H., 1990. A simple derivation of the time-dependent convective diffusion equation for surfactant transport along a deforming interface. Phys. Fluids A 2, 111–112.
Stone, H.A., 1993. An interpretation of the translation of drops and bubbles at high Reynolds numbers in terms of the vorticity field. Phys. Fluids 5 (10), 2567–2569.
Takagi, S., Matsumoto, Y., 2010. Surfactant effects on bubble motion and bubbly flows. Annu. Rev. Fluid Mech. 43, 615–636.
Takagi, S., Uda, T., Watanabe, Y., Matsumoto, Y., 2003. Behavior of a rising bubble in water with surfactant dissolution : 1st report, steady behavior. Trans. Jpn. Soc. Mech. Eng. Ser. B (Japanese) 69 (686), 2192–2199. http://dx.doi.org/10.1299/kikaib.69.2192.
Takemura, F., Yabe, A., 1999. Rising speed and dissolution rate of a carbon dioxide bubble in slightly contaminated water. J. Fluid Mech. 378, 319–334.
Wang, Y., Papageorgiou, D.T., Maldarelli, C., 2002. Using surfactants to control the formation and size of wakes behind moving bubbles at order-one Reynolds numbers. J. Fluid Mech. 453, 1–19.
Xu, J.-J., Li, Z., Lowengrub, J., Zhao, H., 2006. A level-set method for interfacial flows with surfactant. J. Comput. Phys. 212, 590–616.